Heliyon 8 (2022) e09964

Contents lists available at ScienceDirect

Heliyon

journal homepage: www.cell.com/heliyon

Review article

A review on the applications of zinc tungstate ($ZnWO_4$) photocatalyst for wastewater treatment

Hassana Ladio Abubakar [a,c], Jimoh Oladejo Tijani [a,d], Saka Ambali Abdulkareem [b,d], Abdullahi Mann [a], Saheed Mustapha [a,d,*]

[a] Department of Chemistry, Federal University of Technology, PMB, 65, Minna, Niger State, Nigeria
[b] Department of Chemical Engineering, Federal University of Technology, PMB, 65, Minna, Niger State, Nigeria
[c] Department of Chemistry, Nile University of Nigeria, Airport Road, Jabi, Abuja, Nigeria
[d] Nanotechnology Research Group, African Centre of Excellence on Food Safety and Mycotoxins, Federal University of Technology, PMB 65, Bosso, Minna, Niger State, Nigeria

ARTICLE INFO

Keywords:
Nanoparticles
Photocatalyst
Doping
Bandgap
Pollutants

ABSTRACT

The monoclinic wolframite-phase structure of $ZnWO_4$ materials has been frequently synthesised, characterised, and applied in optical fibres, environmental decontamination, electrochemistry, photonics, catalysis, and not limited to magnetic applications. However, the problems of crystal growth conditions and mechanisms, growth, the crystal quality, stability, and the role of synthesis parameters of $ZnWO_4$ nanoparticles remain a challenge limiting its commercial applications. This review presents recent advances of $ZnWO_4$ as an advanced multifunctional material for Industrial wastewater treatment. The review also examines the influence of the synthesis parameters on the properties of $ZnWO_4$ and provides insight into new perspectives on $ZnWO_4$-based photocatalyst. Many researches have shown significant improvement in the efficiency of $ZnWO_4$ by mixing with polymers and doping with metals, nonmetals, and other nanoparticles. The review also provides information on the mechanism of doping $ZnWO_4$ with metals, non-metals, metalloids, metals oxides, and polymers based on different synthesis methods for bandgap reduction and extension of its photocatalytic activity to the visible region. The doped $ZnWO_4$ photocatalyst was a more effective and environmentally friendly material for removing organic and inorganic contaminants in industrial wastewater than ordinary $ZnWO_4$ nanocrystalline under suitable growth conditions.

1. Introduction

As time passes, global industrialization is continuously evolving, thus increasing the need for nanotechnology in most fields (Aghalari et al., 2021). Much attention has been paid to developing techniques that could be used generally to produce different energy sources and improve the quality of human lives. On the one hand, fossil fuels have served as the world's most important energy source for decades. However, due to increasing population and dependency, the unrestrained consumption of fossil fuels has led to an excessive increase in environmental pollution and global warming. The adverse effects of environmental pollution and global warming have led to the demand for sustainable and clean energy sources (Hu et al., 2015; Yesuraj and Suthanthiraraj, 2019). Gold and silver nanoparticles were first used in the 9th century to add glittering effects to home utensils; this was done during the Mesopotamia age. In his famous publication "Experimental Relations of Gold and Other Metals to Light," Michael Faraday gave rise to the scientific introduction of nanotechnology (Faraday 1987). The term nanotechnology was first used in 1959 by Richard Feynman; at this point, the growth of nanotechnology began (Singh et al., 2011). Nanotechnology is the process whereby materials are used at the atomic level utilizing combining biological, chemical, and engineering approaches (Cauerhff and Castro, 2013).

As a result of the finite number of atoms in each crystalline core and the cumbersome fraction of particles residing on the surface, nanoscale materials have been studied for decades; they are also known to have unique properties (Hosseinpour-Mashkani et al., 2016). Inorganic-based nanomaterials involve various metal and metal oxide nanomaterials such as cadmium, aluminium, lead, silver, and gold, while metal oxide-based inorganic nanomaterials include copper magnesium aluminium oxide ($MgAl_2O_4$), zinc oxide, titanium dioxide, and iron oxide. Organic-based

* Corresponding author.
E-mail address: saheedmustapha09@gmail.com (S. Mustapha).

https://doi.org/10.1016/j.heliyon.2022.e09964
Received 10 January 2022; Received in revised form 17 March 2022; Accepted 12 July 2022

nanomaterials are also made from organic materials other than carbon, such as micelles, liposomes, cyclodextrin, and dendrimers. These are examples of carbon-based nanomaterials, single-walled and multi-walled carbon nanotubes, carbon fibre, carbon black, graphene, fullerene, and activated carbon. Lastly, composite-based nanomaterials are a combination of metal oxide-based, carbon-based, metal-based, and organic-based nanomaterials; they are known to have complicated structures like a metal-organic framework (Majhi and Yadav, 2021). The advantages of these materials include cheap and effective wastewater treatment (Gautam et al., 2020), quick and high-efficiency degradation of a wide range of organic pollutants, strong mechanical properties, and chemical stability (Mendes-Felipe et al., 2022). Furthermore, these materials exhibited fast oxidation with no polycyclic and sludge product formation.

Photocatalysis has the advantage of completely mineralize organic pollutants more than other conventional treatment methods such as coagulation, flocculation, co-precipitation, and even precipitation that fail to remove highly toxic pollutants even at low concentrations (Enesca, 2021). There are two main groups of advanced oxidation processes for wastewater treatment: homogenous light-induced technology involving the application of ozonation (UV/O_3 and $UV/O_3/H_2O_2$) and photo-Fenton processes ($UV/Fe^{2+}/H_2O_2$). During the photo-Fenton process, photolysis of H_2O_2 mediated by UV reduction of Fe^{3+} ions and Fe^{2+} ions generated the hydroxide radicals (oxidative species). For Fe^{3+} ion to exist as $Fe(OH)^{2+}$, the $^{\cdot}OH$ photogeneration requires the system to have a maximum pH of 3. The design of homogenous photocatalysts is done so that an optimum light intensity distribution is done simultaneously, and reagents are mixed in a homogenous manner.

In the case of heterogeneous photocatalysis such as $ZnWO_4$, solid catalysts/semiconductors are utilized to remove organic pollutants under light irradiation due to redox reactions in photogenerated charge carriers. The mechanism is divided into three significant steps, generation of charge carrier pairs under irradiation, photogenerated charge carriers migrating on the surface of the catalyst, and initiation of the redox reaction by oxidative ($^{\cdot}OH$) and superoxide ($^{\cdot}O_2^-$) radicals (Enesca, 2021). For instance, Alshehri et al. (2018) investigated that $ZnWO_4$ was used as a photocatalyst to degrade MB dye, and they reported the formation of hydroxy and super-oxide free radicals oxidized the dye molecules to form inorganic minerals. The organic molecules by the photogenerated electron holes can also occur while hydroperoxyl radicals ($^{\cdot}OOH$) and H_2O_2 are produced by the subsequent reactions, which occur between $^{\cdot}O^{2-}$ and H^+. This heterogeneous photocatalytic process induces the mineralization of organic pollutants (CO_2 and H_2O). Depending on the process's efficiency, the pollutant's composition, and its structure, additional products such as acids and salts can be formed (Enesca, 2021).

Exploration into photocatalysis has shown how UV-light, visible light, and solar irradiation can be utilized effectively to reduce environmental pollution (Zhang et al., 2014a,b). Electron-hole pairs are produced when photon energy more prominent than the band gap of the semiconductor used to illuminate the semiconductor; this then leads to the formation of electron-hole pairs $^{\cdot}OH$ (hydroxyl radical) when the generated electrons and holes react with H_2O and molecular oxygen on the surface of the crystal (Zhang et al., 2014a,b). Since $PbWO_4$ was discovered to be capable of photo-catalytically splitting H_2O, H_2, and O_2, $ZnWO_4$ has piqued the interest of many researchers (Saito et al., 2004). With oxygen ions deposited around the tungsten, $ZnWO_4$ forms an insulated $[WO_6]$ octahedron coordination with an asymmetric shape showing its local atomic structures with a monoclinic wolframite-type structure with the space group P2/c (He et al., 2016). This is an essential inorganic ternary oxide material as it has been known to crystallize as a scheelite structure depending on the ionic radius (Chena et al., 2017). However, W clusters form a network because they are more stable, which leads to forming the covalent nature of W–O bonds. In forming electron-hole pairs associated with a charge separation process and dipoles, the WO_6 clusters act as electron receptors. Thus, the oxygen vacancies in the Zn/W clusters can transfer electrons to the tungsten cluster and thus form permanent dipoles (Gouveia et al., 2018). The Zn and W vacancies act as hole traps because they are negatively charged (Zhai et al., 2019). During the UV irradiation of $ZnWO_4$, the conduction band electrons generated are transferred to Ag nanocrystallite due to the Schottky barrier at $Ag/ZnWO_4$, which aid the charge carrier separation (Li et al., 2020a,b).

Different researchers have provided detailed and in-depth information, including improving $ZnWO_4$ as the next-generation catalysts for wastewater treatment. For instance, Gouveia et al. (2018) demonstrated that the overall performance of $ZnWO_4$ nanoparticles was linked to the exposed surfaces of materials, their functional properties, and morphological structures; however, the authors failed to explain the concept of binary and multiple doping effects of $ZnWO_4$. According to the first-principle approach, the photocatalytic activity of $ZnWO_4$ depends on the intrinsic atomic properties and the electronic structure of the incomplete surface clusters of the exposed surfaces of the morphology. The authors found that the surface clusters in the morphology controlled the intrinsic atomic properties of the metal oxide in question.

Furthermore, Geetha et al. (2021a) prepared $ZnWO_4$ nanoparticles via the co-precipitation method for the photocatalytic degradation of methylene blue (MB). The highest dye removal (81 %) was observed for $ZnWO_4$ nanoparticles prepared with 30 cm^3 distilled water. Also, the performance of $ZnWO_4$ depended on the volume of the solvent (30–90 mL) and band gap energy (3.19 eV–3.16 eV), which was evidence of reduced interaction between metal and oxygen orbital.

The members of the tungstate family have, over the years, been used for the mineralization of organic pollutants under UV (Rahmani and Sedaghat, 2019) and sunlight (Paliki et al., 2016) irradiation. However, the photocatalytic strength of $ZnWO_4$ stand-alone is not strong enough (Rahmani and Sedaghat, 2019). The enhancement of the photocatalytic activity of semiconductor $ZnWO_4$ for practical applications has deeply been considered for the degradation of contaminants. This has been the goal of many industries and scientists interested in environmental pollution control. However, a couple of approaches have been reported to further increase the properties of $ZnWO_4$ nanoparticles for wastewater treatment.

Despite intensive literature on $ZnWO_4$, a comprehensive review paper on the photocatalytic mechanism of the $ZnWO_4$ nanoparticles doped with metals and nonmetals, binary-doping and multiple-doping, is still rare. In this vein, the review paper provides detailed information on different synthesis methods, the roles of synthesis parameters on the morphological and textural properties, and the mechanism of doping of $ZnWO_4$. Furthermore, the paper presents insight into recent studies on the photocatalytic and antimicrobial efficiencies of $ZnWO_4$ for wastewater treatment. The limitations of $ZnWO_4$ and an overview of future perspectives are also provided.

2. Different synthesis methods

Different methods have been used to prepare $ZnWO_4$ nanoparticles, including microwave-assisted, co-precipitation, hydrothermal, and sol-gel methods, and they are discussed in the ensuing sections.

2.1. Microwave-assisted, microwave-solvothermal, and microemulsion methods

Over the years, a microwave-assisted hydrothermal or ionic liquid-assisted hydrothermal method was used to synthesize $ZnWO_4$ nanoparticles. Garadkar et al. (2013) successfully presented a quick method that utilizes very little energy, known as the microwave-assisted technique. The $ZnWO_4$ nanoparticles synthesized in this manner were characterized, and the results obtained demonstrated the photocatalytic strength of nanoparticles in the degradation of both aqueous Rhodamine B (RhB) and Methylene Blue (MB) samples; the band gap and particle size were found to be 3.4 eV and 10 nm, respectively. Neto et al. (2020) employed a microwave-assisted hydrothermal method, where $ZnWO_4$ nanoparticles were synthesized at 140 °C and a pressure of 2 atm. This process involved using different concentrations of polyvinylpyrrolidone

(PVP) as a precursor material. It was observed that the higher the hydrothermal treatment time, the better the crystallinity of $ZnWO_4$ powders and the higher its photocatalytic activity, with an average band gap energy of 3.7 eV and a diameter ranging between 3.1-3.4 nm. Also, a highly effective low-temperature ionic liquid-assisted hydrothermal method was used to prepare $ZnWO_4$, where the effects of various operational parameters were also examined, and it was found that the degradation efficiency was 90 % all within 120 min, the nanoparticles synthesized were in the monoclinic wolframite phase with a grain size of 23nm and a band gap of 4.0 eV (Pavithra et al., 2021). $ZnWO_4$ nanoparticles have been synthesized sonochemically, as reported by Rahnamaeiyan et al. (2015), where the precursor solutions were treated with ultrasonic irradiation using a power source of 50 W. The synthesized nanoparticles exhibited ferromagnetic behaviour, and the nanoparticles had a high potential to be used as a photocatalyst under UV irradiation with a band gap of 2.37 eV and a particle size of between 85-90 nm. XRD analysis showed that the $ZnWO_4$ nanoparticles prepared via this route were high purity.

$ZnWO_4$ nanocrystals with controllable shapes have been synthesized using the microwave-solvothermal method. Wang et al. (2017) used the solvothermal synthesis method, where formic acid was utilized for the non-stoichiometry and kinetic size control; this was done at 160 °C. During this research, the surface composition disorder of multi-component oxides was investigated, which contributed to a better understanding of the formation of ZnWO4 nanoparticles with a bandgap of 3.47–3.77 eV and particle size of 20 nm.

The microemulsion method is thermodynamically stable and optically clear dispersion of immiscible solvents, which are stabilized in surfactants. Water droplets comprising the metal precursor are stabilized with a surfactant throughout this technique, and these droplets act as nanoreactors, preventing excessive growth and nanoparticle agglomeration. Emsaki et al. (2018) used the surface-assisted microemulsion method to synthesize ZnO–$ZnWO_4$ nanocomposite, and it was discovered that increasing the amount of $ZnWO_4$ resulted in an increase in the grain size of the nanocomposite as well as a shift in the energy band gap value from 3.2 - 3.16 eV and had a particle size within the range 40–70 nm. Finally, the photocatalytic activity of the nanocomposite was highest (96 %) in the presence of 30 % $ZnWO_4$ in the composite.

Another researcher developed a dependable method for producing cryogenic phonon detectors using scintillating crystals of $ZnWO_4$. The findings of this study were used to assess the effect of thermal and mechanical treatment on the light output of scintillating crystals. A $ZnWO_4$ phonon detector prototype with a thermometer was also created, and it has shown promising results used in the direct dark matter search experiment (Bavykina et al., 2009). In summary, $ZnWO_4$ has a wide range of applications in many other fields, such as humidity sensors (Arularasu and Sundaram, 2016), optical fibres (Ede et al., 2015), environmental decontamination and disinfection (He et al., 2020), microwave applications (He at al. 2016), photoluminescence (Kim et al., 2011), photovoltaic property (Neto et al., 2020), electrochemistry (Seong et al., 1993), photonics (Tang et al., 2014), catalysis (Yang et al., 2016a), supercapacitors (Yang et al., 2016b) and magnetic applications (Zhu et al., 2012). The $ZnWO_4$ as photodegradation and photoluminescence material has been a significant concern to researchers. Sivaganesh et al. (2020) observed that a higher energy bandgap of $ZnWO_4$ dried at 120 °C resulted from the disappearance of the intermediary energy level between the conduction band and valance band. On the contrary, they reported that $ZnWO_4$ calcined at 800 °C possessed a low bandgap. This disparity allowed several defects between the conduction band and valance band. Thus, these structural defects influence photocatalytic and photoluminescence activities.

2.2. Co-precipitation method

Another technique used was co-precipitation, also known as the solid-state analogue technique, in which an inorganic salt is obtained using a precipitating agent. This method aids in bringing cations close together in the reaction medium, as demonstrated by Geetha et al. (2021b), who obtained $ZnWO_4$ nanoparticles by dissolving 0.3 M sodium tungstate in 50 mL of distilled water, and then adding 0.3M zinc chloride dissolved in 50 mL of water dropwise, and analyzing the final product with FE-SEM, FTIR, UV-VIS, and XRD. $ZnWO_4$ nanoparticles had a bandgap of 3.16 eV and a 30–65 nm particle size, respectively. This method is also referred to as a sol-gel process side-branch. There is also the combustion synthesis; here, the precursors are mixed, after which the formed gel is burnt via heating in air at 250 °C, the formed nanoparticles were characterized and applied for the degradation of methylene blue dye in a quartz reactor, and the nanoparticles synthesized were pure crystalline sanmartnite. The crystallite size was calculated to be between 24-38 nm, and the nanoparticles exhibited the highest photocatalytic activity at 600 °C with 94 % degradation by the nanoparticles having a surface area of 27.4 m^2/g (Grabis et al., 2012). The co-precipitation method is classical, inexpensive, and simple since it involves precipitating a metal, usually in hydroxide, from a salt precursor using a base as a solvent. The controlled release of cations and anions regulates the nucleation and particle growth kinetics during this process. This facilitates the creation of monodispersed nanoparticles. However, controlling the chemical homogeneity and particle size during metal oxide precipitation is extremely difficult. In general, pH, temperature, and the concentration of reactants and ions all significantly impact the precipitation process (Sharma et al., 2017). Because it involves a soft chemical route to mixed oxide materials, this method is also known as a side-branch of the sol-gel process. The first step in this process is the dissolution of precursor materials in a common solvent; the second step is introducing a precipitating agent into the system to form a homogeneous organic solid in a single phase.

Furthermore, the precipitate formed at a very high temperature must be decomposed to produce the target mixed oxide material. The starting materials, in this case, can be simple metal salts that can be easily dissolved in water or an appropriate solvent; this process helps to lower the temperature of decomposition of the end products; it also helps to keep the required cations together in a reaction medium (Babooram, 2008). Geetha et al. (2021a) used the co-precipitation method to create $ZnWO_4$ nanoparticles, with the starting solution, i.e., the volume of distilled water used to dissolve the precursors, varying between 30 and 90 mL. This research focused on checking the effect of solvent concentration on the efficiency of nanoparticles; 0.408 g and 0.989 g of zinc chloride and sodium tungstate, respectively, were used as sources of Zn^{2+} and WO^{2-}_4. The XRD results confirmed the formation of well-defined diffraction peaks indicating the monoclinic with wolframite structure of the synthesized $ZnWO_4$ product. The photoluminescence analysis reveals bands associated with the charge transfer transition in WO_4^{2-} groups, in which oxygen (O) 2p electron enters one of the empty tungsten (W) 5d orbitals. The WO6 octahedral structure acts as the luminescent centres in the matrix, as well as the charge transfer state (CTS) transition between the O 2p orbitals and the empty d orbitals of the central W6+ ions, which causes the bluish-green spectral species effect that $ZnWO_4$ nanoparticles have (Amouzegar et al., 2015). Due to an increase in the electron-hole pair recombination rate on the surface of the $ZnWO_4$ nanoparticles, a 70 mL sample had a substantially greater absolute luminescence intensity than the other samples. The FE-SEM image of the $ZnWO_4$ nanoparticles produced with 30 mL of solvent shows the nanoparticles with hexagonal cross-sections distributed in a homogeneous manner, which helped to enhance the intensity of the photoluminescence. However, the FE-SEM of the sample prepared using 90 mL of solvent showed smaller particles that are tightly packed together and form a dense structure. This indicates that the amount of solvent affects the morphology of the obtained $ZnWO_4$ nanoparticles.

An ultrasonic-assisted co-precipitation method has been applied in the co-precipitation synthesis of $ZnWO_4$ nanoparticles as a result of an inefficient co-precipitating for utilization in large-scale industrial settings. This ultrasonic-assisted co-precipitation method has helped address the issue and improved reaction rates (Iskandar et al., 2014). The

technique seems to overcome the disadvantage of using the co-precipitation method alone because it is eco-friendly, low-cost, and the entire process can be carried out at room temperature. The synthesis process involved stirring zinc nitrate hexahydrate and sodium tungstate dehydrate for 1 h and sonication of the mixture for 1 h before washing in ethyl alcohol. The synthesized $ZnWO_4$ nanoparticles were characterized using XRD, and the results showed that $ZnWO_4$ nanoparticles were monoclinic. The XPS analysis revealed peaks corresponding to Zn 2p, O 1s, and W 4f 2^+, 6^+, and 2^+ electronic states of $ZnWO_4$ nanoparticles. SEM images showed that the $ZnWO_4$ nanoparticles were slightly agglomerated and confirmed that the nanoparticles obtained were nanosized. According to EDX analysis, the Zn, W, and O percentages were 25.2 %, 54.5 %, and 20.2 %, respectively. According to the TEM results, the nanoparticles were between 80 and 50 nm in size. The synthesized nanoparticles' selected area diffraction (SAED) pattern confirmed that they were highly crystalline. Lastly, the synthesized nanoparticles successfully detected furazolidone in biological samples (Rajakumaran et al., 2021). Other research has been done to synthesize $ZnWO_4$ for different applications, as seen in Table 1.

Overall, the co-precipitation method has been successful for synthesizing pure and crystalline $ZnWO_4$ nanoparticles and is also effective for the degradation of pollutants.

2.3. Hydrothermal synthesis

Over the years, hydrothermal synthesis was used to create a variety of nanomaterials such as metal oxides and their composites. The general reactions usually occur in aqueous media at ambient temperatures and pressures, and they are generally heterogeneous. During this process, the precursors are dissolved in water and mixed to form aqueous mixtures of the precursors. The solution is placed in a sealed stainless container, and the precursors are heated above the boiling points of the water. This process involves increasing the pressure within the autoclave and going above the atmospheric pressure. This process that combines high temperature and pressure produces a one-step process that produces highly crystalline nanomaterials. Unfortunately, this method has a meager yield of nanomaterials compared to the other methods that have also been utilized. The basis of the hydrothermal method involves a high vapour pressure and a high temperature in an aqueous solution, hence the name "hydro"- "thermal." This technique generally utilizes a hydrothermal autoclave reactor. The hydrothermal method is extensively used due to various advantages like ease of temperature, pressure, and pH, leading to different morphologies of nanomaterials (Ahmad et al., 2018). Also, this method is beneficial for synthesizing highly crystalline nanoparticles, which are generally unstable at high temperatures.

A facial hydrothermal method was used to fabricate boron (B) doped $ZnWO_4$ nanorods by Liu et al. (2017), and the resulting nanoparticles were characterized where the XRD results showed that the nanoparticles were monoclinic wolframite tungstate phase and that as the concentration of B increased, the intensity of the peaks decreased. On the other hand, TEM analysis shows that the products were nanorods of 50–200 nm in length and 5–8nm in diameter. The BET analysis of the samples revealed the formation of a mesoporous material of type IV isotherm and the hysteresis loop type H3 As the crystal size decreased from 12.5, 12.3,

Table 1. Co-precipitation synthesis of $ZnWO_4$ nanoparticles.

Method	Reaction Conditions	Characterization Technique	Major Findings	References
Co-precipitation	$ZnCl_2$, Na_2WO_4, $Tbcl_3$, and ethylene glycol (EG). Dried at 60–70 °C for 24 h.	XRD, SEM, EDX, FTIR and UV-VIS.	The XRD results showed that the $ZnWO_4$:Tb^{3+} phosphors analyzed were spherical and had a diameter between 8-12 nm. As the concentration of the Tb^{3+} ion increased, the crystallinity of the samples decreased due to the substitution of Zn^{2+} with Tb^{3+}; the crystallite size decreased to 8.4 nm from 11.3 nm as the concentration of the dopant ion went from 1 to 3%. The crystallite remained the same between 3 and 5%, later increasing to 10%, and was highest at 12% at 9.7 nm and 11.0 nm. FTIR results show that the nanoparticles had a peak at 835 cm^{-1}, indicating the presence of Zn–O–W bonds. TEM studies showed the $ZnWO_4$:Tb^{3+} phosphors as having a spherical morphology without agglomeration.	Singh et al. (2019)
Co-precipitation	$Zn(CH_3CO_2)_2.5H_2O$, $NaWO_4.2H_2O$, HMTA, PVP, and SDS. pH = 10. Dried at 120 °C for 5 h.	XRD, SEM, EDX, XPS, and TEM	The nanostructures obtained were crystalline with 16, 14, 30, and 31 nm crystallite sizes. SEM analysis showed that $ZnWO_4$:PVP and $ZnWO_4$:SDS nanostructures were spherical while $ZnWO_4$:HMTA nanostructures were agglomerated. Without any surfactants, $ZnWO_4$ had an irregular morphology. $ZnWO_4$:PVP had the best photocatalytic activity. EDX mapping showed sharp peaks corresponding to Zn, W, and O.	Sivaganesh et al. (2020)
Co-precipitation	$Zn(NO_3)_2.6H_2O$ and $NaWO_4.2H_2O$. Dried at 80 °C for 12 h.	XRD, SEM, and DSC	A central composite design (CCD) was used where XRD results were compared with those of an actual $ZnWO_4$. The $ZnWO_4$ nanoparticles obtained were spherical from the SEM images, and the optimum conditions for synthesis at the smallest nanoparticles size are 73 °C temperature, 1.30 mol weights of precursors, and a pH of 7. The average particle size of the nanoparticles obtained was 28nm.	Abdolrahmany et al. (2015)
Co-precipitation	$ZnCl_2$, $NaWO_4.2H_2O$. . Dried at 80 °C for 6 h.	XRD, FESEM, FTIR and UV-VIS	XRD results showed that an increase in temperature (300 °C–500 °C) led to an increase in the crystallinity of the nanoparticles as the crystallite sizes vary from 30-65 nm. SEM studies revealed well-dispersed spherical solid shells with a uniform size distribution of 300 nm and a nanoplate morphology, some level of agglomeration was observed when the calcination temperature was increased to 400 °C from 300 °C. At the same time, a nanoplate morphology was observed when the temperature increased to 500 °C.	Geetha et al. (2021b)
Co-precipitation	$Zn(NO_3)_2.6H_2O$, $NaWO_4.2H_2O$ and $Na_2WO_4.2H_2O$. pH = 9. Dried at 60 °C for 24 h.	XRD, SEM, EDX, XPS, and PL	The $ZnWO_4$ precursor had an irregular shape; the average grain size increased as the annealing temperature increased. The precursors had an average grain size of 80 nm. The annealed samples' diffraction peaks were indexed to the monoclinic phase. The intrinsic defects in $ZnWO_4$ were used to create colour-tunable light-emitting phosphorus; this work presents a novel method of tuning the emissions obtained due to rare earth metal doping of $ZnWO_4$ phosphorus.	Zhai et al. (2019)

11.9, 10.9, 9.3, and 7.7 for $ZnWO_4$, B (0.35 wt%)/$ZnWO_4$, B (1.04 wt %)/$ZnWO_4$, B (1.73 wt%)/$ZnWO_4$, B (2.42 wt%)/$ZnWO_4$ and B (3.11 wt %)/$ZnWO_4$, the surface area increased from 21.3, 22.0, 22.0, 30.3, 38.2 and 47.2. Lastly, the average pore diameter was between 30nm and 50nm. Since different samples with different ratios of B were synthesized, the calculated bandgap energy for $ZnWO_4$, B (0.35 wt%)/$ZnWO_4$, B (1.04 wt%)/$ZnWO_4$, B (1.73 wt%)/$ZnWO_4$, B (2.42 wt%)/$ZnWO_4$ and B (3.11 wt%)/$ZnWO_4$ were found to be 3.44, 3.42,3.54,3.56,3.62 and 3.55 eV respectively. It was noticed that doping $ZnWO_4$ with B led to a slight adjustment of the ban structure of $ZnWO_4$, and as the amount of B increased, the bandgap of $ZnWO_4$ increased at first. The highest bandgap was obtained in the case of B (2.42 wt%)/$ZnWO_4$ at 3,62 eV, resulting from the Bursten-Moss shift (Burstein 1954; Moss 1954). When the B content was low, the B^{3+} did not replace W^{6+} in $ZnWO_4$, B (0.35 wt %)/$ZnWO_4$; however, when the content was raised to 1.04 wt%, B^{3+} was produced by the level of the hole defect instead of W^{6+}. As soon as the B content increased to 3.11 wt%, the bandgap decreased to 3.55 eV Table 2 presents other research that has been done over the years on the synthesis of $ZnWO_4$ for different applications using the hydrothermal synthesis method.

$ZnWO_4$ nanomaterials synthesized using the hydrothermal method were pure; however, the structure of synthesized nanorods tends to vary from tubular to needle-like depending on the treatment time. This method can be carried out at different pH levels between 3-13.

2.4. Sol-gel method

This is also called chemical solution deposition; it entails hydrolysis and polycondensation, gelation, aging, drying, densification, and crystallization. It is a highly effective method for synthesizing nanoparticles with modified surfaces. Grossin (2021) describe this method as involving the hydrolysis of the precursor in acidic or basic mediums and the polycondensation of the hydrolyzed. Rahmani and Sedaghat (2019) studied the nature of the $ZnWO_4$ nanoparticles obtained from this study. The nanoparticles were synthesized by adding 30mL ethanol and 3 mL HCL into a mixture of zinc acetate dropwise, while sodium tungstate in deionized water was added to 20 mL of ethanol in a dropwise form. Both solutions were mixed vigorously, after which urea was added to the zinc acetate and sodium tungstate mixture. The nanoparticles synthesized were characterized as well, where it was observed that the band gap energy was 3.20 eV. The nanoparticles synthesized had an average diameter of between 26-78 nm. The N-doped $ZnWO_4$ nanoparticles had a higher photocatalytic efficiency as they degraded 99.1 % and 97.62 % MB under UV light after 120 and 240 min, respectively. The synthesis occurred at a pH of 6 and a temperature of 500 °C. Another effective method is the sol-gel method, which involves transforming a solution from a liquid (sol) to a solid (gel) phase. In this case, inorganic metal salts or metal-organic compounds such as alkoxides are used as base materials, and the colloidal suspension is typically formed through a series of hydrolysis and polymerization reactions (sol). Thin films are durable and have various properties, usually poured on a substrate by dip coating or even spin-coating (Greco et al., 2011; Grossin, 2021). The delivery of the final metal oxide involves a few sequential steps in which the corresponding metal precursor undergoes rapid hydrolysis to synthesize the metal hydroxide solution. Condensation occurs immediately after, resulting in the formation of three-dimensional gels. Lastly, the obtained gel is subjected to a drying process where the resulting function is converted to xerogel or aerogel based on the method in which it was dried

Table 2. Hydrothermal synthesis of $ZnWO_4$ nanoparticles.

Method	Reaction Conditions	Characterization Technique	Major Findings	References
Hydrothermal	$Zn(NO_3)_2.6H_2O$, $NaWO_4.2H_2O$, $Al(NO_3)_3.9H_2O$ and $Ni(NO_3)_2.6H_2O$. pH = 9. In an autoclave at 160 °C for 12 h.	XRD, UV-VIS, FE-SEM, FTIR, and XPS	FE-SEM results show that the nanoparticles synthesized had an acicular morphology, and the pore size of the nanoparticles decreased with the loading of NiAl-LDH. Also, ZWLDH-20 has a rough surface. FTIR results show that the nanoparticles had a peak at 835 cm^{-1}, indicating the presence of Zn–O–W bonds. From the XPS data, the binding energies of ZWLDH were 37.8 and 35.7 eV for W $4f_{s/2}$ and W $4f_{3/2}$.	Zhao et al. (2020)
Hydrothermal	$Zn(NO_3)_2.6H_2O$, NH_4OH and H_2WO_4. pH = 7, In an autoclave at 200 °C for 2 h.	XRD, FTIR, UV-VIS, DRS, SEM, TEM, and XPS.	XRD results revealed that the nanoparticles were of a crystalline phase, the SEM images obtained displayed the rod-like morphology, and the $ZnWO_4$ precipitated first acted as a seed for the growth of ZnO onto its surface. The formation of the heterostructure Zn–$ZnWO_4$ increased the lifetime of the electron-hole pair.	Carvalho et al. (2019)
Hydrothermal	$Zn(NO_3)_2.6H_2O$, $NaWO_4.2H_2O$. pH = 9. In an autoclave at 180 °C for 3 h, 6 h, 12 h and 24 h.	XRD, SEM, and UV-VIS.	XRD results showed that the diffraction peaks corresponding to $ZnWO_4$ were absent in the hydrothermally treated samples for 24h; instead, ZnO peaks were observed. The sample was treated for 3 h, 6 h, and 12 h; however, it had wolframite $ZnWO_4$. The structures went from tubular (3h) to needle-like (6 and 12 h). At 24 h, a distribution of solid-hexagonal was observed. $ZnWO_4$ catalysts were hydrothermally treated at 180 °C for 12 h at different pH (3, 6, 8, 10, and 13). The optimum conditions for preparing $ZnWO_4$ catalysts were pH 10. They were needle-like in morphology and had the best photocatalytic activity.	Luo et al. (2018)
Hydrothermal	Precursors used were $Zn(NO_3)_2.6H_2O$ and $NaWO_4.2H_2O$ pH = 9. In an autoclave at 180 °C for 24 h.	XRD, SEM, EDX, TEM, and UV-VIS	XRD results demonstrated that the sample was in a pure monoclinic crystalline phase. EDX results also showed that the sample analyzed contained Zn, W, and O. SEM showed rod-like particles with homogenous morphology after 180 min of irradiation, with a particle size of 100 nm. The particles had a length of 100 nm and a width of 30 nm.	Zhao et al. (2016)
Hydrothermal	Precursors used were $ZnCl_2.6H_2O$ and $NaWO_4.2H_2O$ pH = 10. In an autoclave at 180 °C for 24 h	XRD, TEM, BET, UV-VIS	XRD results showed that the nanorods were of high crystallinity. TEM images indicated the homogenous morphology of the nanorods (60–100 nm) with a single crystal structure. High photocatalytic activity of the $ZnWO_4$ Nanorods compared to $CoWO_4$ and $ZnWO_4$ Nanowires (since the nanorods have a higher surface area). The nanorods exhibited a lower rate of recombination of holes and electrons. There was better adsorption of Rhodamine Blue due to higher catalytic active sites.	Zhang et al. (2014a,b)

(Rao et al., 2017). The sol-gel method could be either aqueous or non-aqueous depending on whether water was used and the nature of the solvent, as shown in Figure 1 (Rao et al., 2017).

The sol is then cast into a mould, forming a wet gel, which is then converted into dense materials after drying and heat treatment. When the liquid in a wet gel is extracted under supercritical conditions, an aerogel, a low-density, highly porous material, is formed. When the viscosity of a sol is adjusted, fibre can be obtained. Spray pyrolysis, precipitation, and emulsion methods obtain ultrafine and uniform powders. Tailorable microstructure, ease of compositional modifications, control of stoichiometry of precursor solutions, ease of introducing various encapsulating sensing elements and functional groups, simple and inexpensive equipment, and relatively low annealing temperatures are some of the benefits of the sol-gel process (Rao et al., 2017). Recently, researchers have made several adjustments to the synthesis route of $ZnWO_4$ nanoparticles to produce better and more effective nanoparticles and control the morphology of the nanoparticles. Graphene Oxide (GO) hybridized $ZnWO_4$ nanoparticles were prepared using the sol-gel route; here, factors such as the reaction time and temperature played a considerable role in determining the size and morphology of the nanoparticles. XRD results showed that the diffraction peaks present belong to $ZnWO_4$, while peaks of GO were absent due to the shielding effect of peaks belonging to $ZnWO_4$ over GO peak at 2 theta value 24.5^o indexed to (110) crystal planes. FTIR results presented a sharp peak at 1419 cm-1, belonging to the CO group, the peaks at 1560 cm^{-1} to benzene rings, and a broad and wide peak at 3447 $cm^{-1,}$ which belongs to OH stretching vibrations emanated from the C–OH groups and water. The peak around 1560 cm^{-1} belongs to the GO sheets' skeletal vibration, indicating graphene structure formation. The fingerprint groups, including carboxylic species, epoxy species as well as hydroxyl species, are consistent with the vibrational peaks of GO (C=O at 1734 cm^{-1}, OH deformation at 1400 cm^{-1}, C–OH stretching at 1230 cm^{-1}, C–O–C stretching at 1061 cm^{-1} and lastly the skeletal ring stretch at 1624 cm^{-1}).

The presence of the basic hydroxyl groups in the $ZnWO_4$ sample was further proved when two peaks were observed at 3447 cm^{-1} and 1629 cm^{-1}. This confirmed $ZnWO_4$ to be hydroxylated. UV-VIS (DRS) spectra show the absorbance edge of $ZnWO_4$ around 550 nm, with bandgap energy of the synthesized GO/$ZnWO_4$ as 2.32 eV. Pure $ZnWO_4$, on the other hand, had a bandgap of 3.2 eV; thus, the lower bandgap signifies the ability of GO/$ZnWO_4$ to work well under visible light irradiation. The GO/$ZnWO_4$ nanoparticles were used to synthesize benzaldehydes under a solvent-free condition; this process has an excellent yield. NMR, FTIR, and C-NMR studies were used to prove the formation of benzaldehydes (Paliki et al., 2018). Table 3 presents novel research that has been done over the years on synthesizing $ZnWO_4$ for different applications using the sol-gel synthesis method.

This sol-gel method has been used successfully to degrade organic dyes like methyl orange, phenol red, rhodamine blue, and even methyl blue. The nanoparticles synthesized via this route have been doped with nonmetals under visible light such as nitrogen to improve their efficiencies. This method produces nanoparticles that are very pure and with high crystallinity.

3. Different parameters affecting the nanoparticles

During synthesis, different parameters affect the size, shape, textural properties, and surface area of the nanoparticles. Researchers have proved that adjustments in the parameters have led to a change like the nanoparticles (Somorjai and Park, 2008). Temperature, the concentration of precursor materials used, the concentration of extracts (in the case

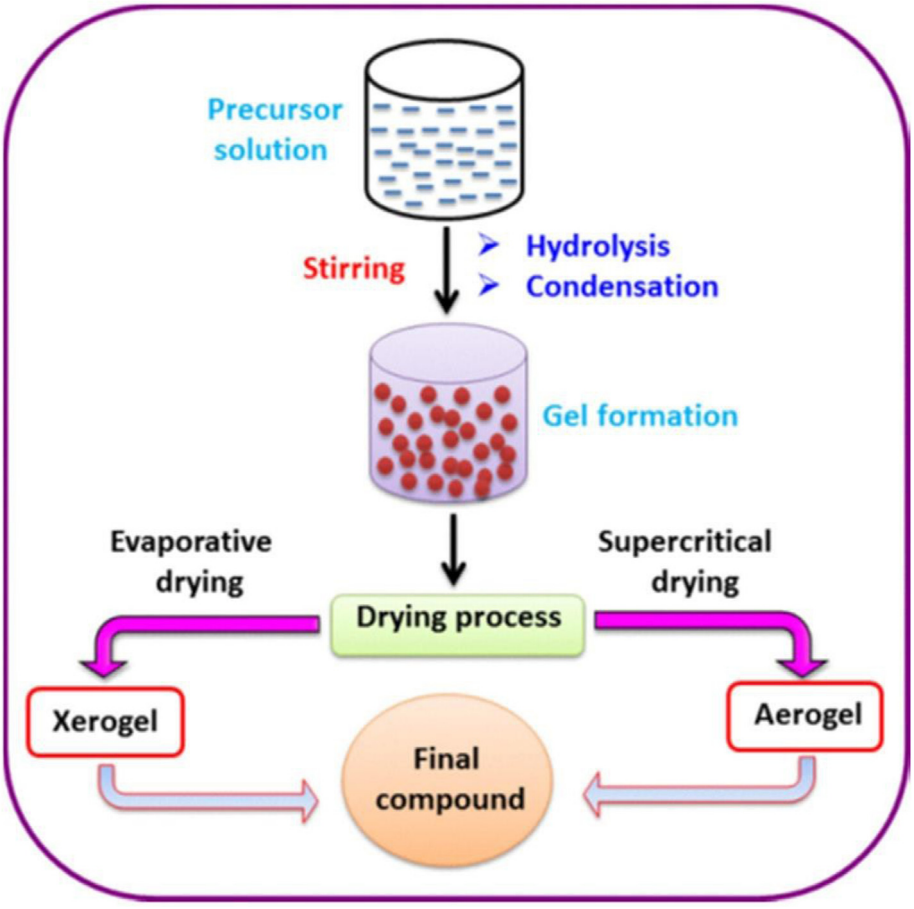

Figure 1. The reaction pathway for the sol-gel method (Rao et al., 2017).

Table 3. Table showing the most recent research that has been done on the sol-gel synthesis of $ZnWO_4$ nanoparticles.

Method	Reaction Conditions	Characterization Technique	Major Findings	References
Sol-gel	$Na_2WO_4.2H_2O$ and $Zn(CH_3COO)_2.2H_2O$. pH = 7, dried at 100 °C for 12h and calcined at 600 °C for 2 h	XRD, SEM, XPS, TEM, and UV-VIS	XRD results showed that the sample analysed was in a monoclinic phase, and the crystallite size was 24.6 nm. SEM/TEM analysis showed that the nanocomposite material had a clear morphology with highly agglomerated, near quasi-spherical/ellipsoidal-shaped particles.	Jaramillo-Pa ez et al., 2021
Sol-gel	$Na_2WO_4.2H_2O$ and $Zn(CH_3COO)_2.2H_2O$. pH = 3, 6, and 8, oven-dried at 80 °C for 2 h and calcined at 400 °C, 500 °C, and 600 °C for 5 h	XRD, SEM, EDS, UV-VIS and FTIR	It was observed that pH and temperature affected the efficiency of the nanoparticles. The diffraction peaks of the samples synthesized at pH 6 were indexed to the pure monoclinic phase. The purest nanoparticles were obtained at 500 °C at pH 6. TEM analysis showed that the nanoparticles synthesized had an average diameter of between 27-78 nm, and the surface area from BET analysis was gotten as 5.8161 m^2g^{-1}	Rahmani and Sedaghat (2019)
Sol-gel	$H_3PW_{12}O_{40}.{}_XH_2O$ (PTA), $Zn(Ac)_2.2H_2O$ and $Sncl_4.5H_2O$. pH = 8, dried at 110 °C for 20h and calcined at 600 °C for 2h	XRD, SEM, UV-VIS and PL	The XRD results showed peaks attributed to hexagonal ZnO, monoclinic $ZnWO_4$, and tetrahedral SnO. The peak of ZnO was sharper than that of SnO and $ZnWO_4$. SEM images showed that small crystallites of the different phases were interwoven, forming nanoclusters. TEM images, however, showed that the size range was between 20-150 nm the bandgap calculated was within the range of 3.10–3.22 eV.	Hamrouni et al. (2015a),b
Sol-gel	$5(NH_4)_2.12WO_3.5H_2O$, $Zn(NO_3)_2.6H_2O$and citric acid. pH = 2–3, dried at 85 °C for 20h and calcined at 550 °C for 3 h	XRD and SEM	The $ZnWO_4$ and $ZnWO_4$/CNTs were both wolframite and tungstate with a crystallite size of 19.63 mm, while that of pure $ZnWO_4$ was 20.93 nm. The SEM images of pure $ZnWO_4$ had irregular shapes, whereas, in the $ZnWO_4$/CNTs composite, CNTs permeated the $ZnWO_4$, improving the electrical conductivity of the nanoparticles. Finally, the $ZnWO_4$/CNTs composite demonstrated remarkable electrochemical properties such as high reversibility capacity, superior rate capability, and cycling stability. The $ZnWO_4$/CNTs composite is a promising anode material for lithium-ion batteries.	Zhang et al. (2014a,b)

of green synthesis), pH of the solution, surfactants used, time, and, in some cases, method or technique used are all factors that influence nanoparticle synthesis (Patra and Baek, 2014).

Several researchers have varied parameters needed to synthesize $ZnWO_4$ nanoparticles to see how each one affects the nature of formed nanoparticles. In most cases, XRD, SEM, TEM, EDX, and FTIR techniques are used to monitor the structural and morphological characterization of the targeted properties within the product (Hosseinpour-Mashkani et al., 2016). A study by Yan et al. (2013) showed that an increase in the reaction temperature up to 180 °C led to an increase in the crystallinity of the synthesized $ZnWO_4$ nanoparticles. The use of surfactants affects the texture of $ZnWO_4$ nanoparticles; here, it was reported that the polyvinylpyrrolidone (PVP), Hexamethylenetetramine (HMTA), and sodium dodecyl sulfate (SDS) were utilized as surfactants where $ZnWO_4$ prepared with PVP and SDS had an apparent morphology and were spherical unlike the nanoparticles formed using HTMA as a surfactant, in which case, the formed nanoparticles will be agglomerated. This analysis went deeper by stating and proving that the $ZnWO_4$ nanoparticles synthesized using PVP even had a smooth surface with a hexagonal plate-like morphology. Using SDS as a surfactant, the $ZnWO_4$ nanoparticles also had a hexagonal plate-like morphology, but the nanoparticles had rough surfaces. The report also stated that HTMA did not produce ZnWO4 nanoparticles with a deformed hexagonal structure of the three surfactants. This is because HTMA acted as a capping agent and was able to control the growth of the $ZnWO_4$ nanoparticles. HTMA nanoparticles also had a non-polyhedral shape. However, $ZnWO_4$:PVP and $ZnWO_4$:SDS produced highly crystalline samples with a monoclinic structure of wolframite. It was observed that both HMTA and PVP acted as capping agents, which prevented the particles from coagulating. Unlike HMTA and PVP, it was observed that coagulation of $ZnWO_4$:SVP was prevented since a hairy layer was formed around the particles due to the long strands in SDS (Sivaganesh et al., 2020). It was also reported that the formed nanoparticles prepared without a surfactant had an unrefined morphology, with a deformed hexagonal shape structure. The utilization of polyethylene glycol (PEG) during synthesis has proven to produce better nanoparticles. $ZnWO_4$ nanoparticles synthesized by Severo et al. (2016) using PEG were assigned the monoclinic phase from the XRD data presented; this means the sample was single-phase. Paliki et al. (2016) also synthesized $ZnWO_4$ nanoparticles for catalytic oxidation. This researcher also used PEG and obtained monoclinic wolframite nanoparticles; this process took place at room temperature. $ZnWO_4$ nanoparticles synthesized by Severo et al. (2016) using (PEG) were assigned the monoclinic phase from the presented XRD data. It was also observed that the nanoparticles obtained had different accumulated pore voids on the surface of the particles due to the agglomeration of the particles. Jaramillo-Perez et al. (2021) found out that without any thermal treatment, the synthesized $ZnWO_4$ nanoparticles were amorphous; after calcination, at 600 °C for 2 h, the nanoparticles became crystalline with a monoclinic phase of sanmartnite $ZnWO_4$. The data presented in the report showed how using Triethylamine (TEA) in place of NaOH during synthesis to adjust the pH 10 led to the ZnO nanoparticles. This research also observed that an increase in temperature beyond 600 °C had little to no effect on the phase of the $ZnWO_4$ nanoparticles formed. TEA also acted as a chelating agent, inhibiting the formation of $Zn(OH)_2$ and polyoxotungstates. This favoured the formation of $ZnWO_4$ nanoparticles in the absence of TEA. pH adjustment results in the formation of $Zn(OH)_4^{2-}$ complex, which now generates Zn(OH)2, leading to ZnO's appearance after calcination. So basically, the presence of TEA destabilizes the chances of formation of $ZnWO_3$ and favours ZnO formation. The precursors involved during this synthesis were sodium tungstate dehydrate and zinc acetate dehydrates, the solutions were mixed vigorously and washed several times, and calcination was done at 600 °C for 2 h. The schematic diagram of the entire process is presented in Figure 2.

Another researcher, Mosleh and Teherinejat (2016), also studied the effects of sodium dodecyl benzene sulfonates, propylene glycol, ethylene glycol, and spherical-shaped $ZnWO_4$ nanoparticles were obtained irrespective of the surfactants. Hosseinpour-Mashkani et al. (2016) also studied the effect of surfactants such as polyethylene glycol (PEG), carboxymethyl cellulose (CMC) as well as polyvinyl alcohol (PVA). Here, it was observed that using propylene glycol as a solvent and CMC as a

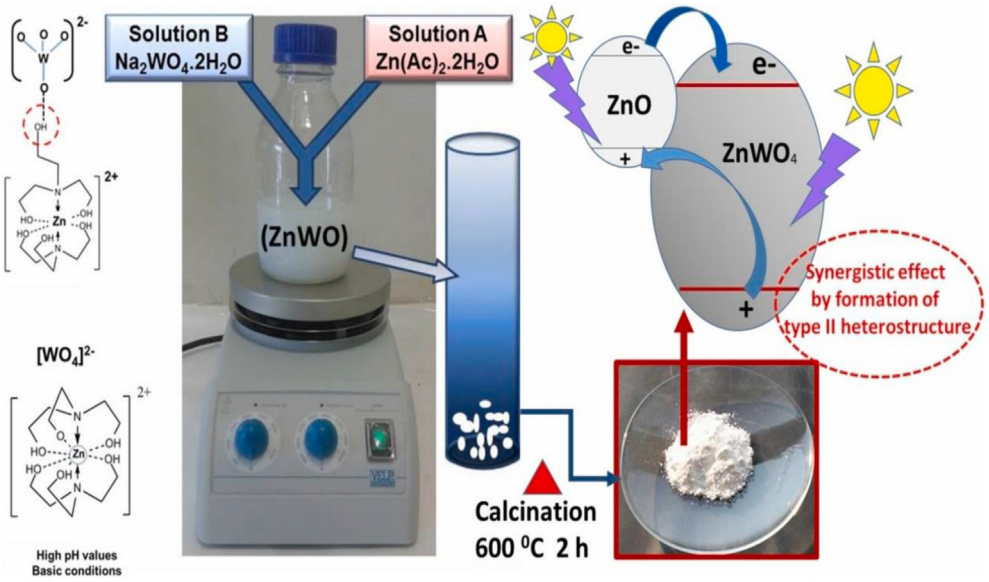

Figure 2. The synthesis of Zn rich $ZnWO_4$ nanoparticles (Jaramillo-Perez et al., 2021).

surfactant led to the formation of the most crystalline nanoparticles compared with the nanoparticles formed using either PEG or CMC as surfactants. Paliki et al. (2016) synthesized pure spherical-shaped $ZnWO_4$ nanoparticles with a monoclinic wolframite structure using ethylene glycol. He et al. (2020) synthesized $ZnWO_4$ nanoparticles using different ethylene glycol concentrations and found that $ZnWO_4$.EG0, $ZnWO_4$.EG50 and $ZnWO_4$.EG65.2 had excellent crystallinity. The XRD data obtained also pointed out the fact that $ZnWO_4$.EG75 had different diffraction peaks. The phase of $ZnWO_4$ nanoparticles synthesized can be altered by regulating the acidity and basicity during the reaction process between 3, 6, and 8, as presented by Rahmani and Sedaghat (2019). This report proved that pure $ZnWO_4$ nanoparticles with the best crystallinity can be obtained by controlling the pH value and maintaining it at 6. This same researcher carried the work further by investigating the effects of variation of calcination temperature (between 400 °C, 500 °C, and 600 °C) on the $ZnWO_4$ nanoparticles synthesized. The authors found that calcination temperature can affect the crystallinity of the nanoparticles. These samples were analyzed, and the results showed that the nanoparticle calcined at 500 °C produced the purest ZnWO4 with no impurities. Still, on temperature variations, Faka et al. (2021) annealed $ZnWO_4$ nanoparticles synthesized at temperatures between 400 °C–800 °C and reported that a single phase of $ZnWO_4$ nanoparticles only formed when the temperature got to 500 °C; it was also noticed that at higher temperatures between 600-800 °C $ZnWO_4$ nanoparticles was fully formed. During this same research, it was observed that the crystallinity of the $ZnWO_4$ nanoparticles increased as the temperature increased, meaning that the crystallinity of the $ZnWO_4$ nanoparticles formed at 500 °C was lower than that of the nanoparticles formed between 600 °C-800 °C. Rahmani and Sedaghat (2019) used the sol-gel approach, while Faka et al. (2021) used an easy solution-based synthesis route. Hao et al. (2017) synthesized $ZnWO_4$ nanoparticles at pH 10.6; the formed nanoparticles had hexagonal wurtzite and monoclinic phases. After synthesis, the nanoparticles were calcined at 750 °C, 850 °C, and 950 °C for 2 h; the researcher observed that the crystallinity increased as temperature increased. An increase in reaction temperature between 250 °C, 300 °C, 350 °C, and 400 °C has also proven effective at enhancing the crystallinity of $ZnWO_4$. They were all found to be monoclinic (Bøjesen et al., 2016). Another study shows how $ZnWO_4$ nanoparticles have been fabricated as a scintillator material using zinc oxide and tungsten oxide through a solid-state reaction at temperatures of 700 °C, 800 °C, and 900 °C, analysis of the XRD patterns obtained showed that all three samples crystallized into pure monoclinic $ZnWO_4$ nanoparticles (Jeong et al., 2020). Pavithra et al. (2021), on the other hand, synthesized $ZnWO_4$ nanoparticles at a lower of about 180 °C for a longer time of 24 h; the nanoparticles obtained were also monoclinic wolframite in nature. Mehdi et al. (2015) proposed that the size of $ZnWO_4$ nanoparticles is strongly affected by experimental factors such as Zn^{2+} and WO_4^{2-} ion concentration (M), Zn^{2+} feed flow rate (mL/min) to the WO_4^{2-} solution as well as temperature. These conditions were optimized using the orthogonal array design (OAD); it was then concluded that 0.1 M of Zn^{2+} and WO_4^{2-} ion concentration (M), 2.5 mL/min Zn^{2+} feed flow rate (mL/min) to the WO_4^{2-} solution and 60 °C temperature were the optimum conditions. The Zn^{2+} and WO_4^{2-} ion concentration (M), Zn^{2+} feed flow rate (mL/min) to the WO_4^{2-} solution, and temperature obtained at these conditions were monoclinic with a hydrated structure. Time has also proven to be an essential factor to be considered when synthesizing nanoparticles, as Neto et al. (2020) discovered that the crystallite size of a nanoparticle was greatly influenced by the increase in hydrothermal treatment time. It was also reported that increasing the time from 5 – 120 min, the crystallite size went from 39.83 to 217.18 Å, the sample treated for 120 min exhibited the highest crystallization at 100 %, and after 120 min, there were no notable changes in the crystallinity of the $ZnWO_4$ nanoparticles at a treatment time higher than 120 min.

It has been observed that the sizes of nanoparticles tend to vary depending on several factors; this was proved by many researchers, including Hosseinpour-Mashkani et al. (2016), who also studied the effect of surfactants on the size of nanoparticles, using PEG led to the synthesis of smaller sized nanoparticles with a good size distribution. Furthermore, PEG was used as a surfactant for the synthesis of $ZnWO_4$ nanoparticles at 500 °C by Geetha et al. (2019), and it was observed that an increase in the concentration of PEG by 0.3 g, 0.5 g, 0.7 g, and 0.9 g led to the formation of $ZnWO_4$ nanoparticles with corresponding crystallite sizes: 70 nm, 56 nm, 65 nm, 60 nm, and 65 nm respectively. The authors further explained that PEG concentration played a vital role in controlling the nucleation and growth of $ZnWO_4$ nanoparticles. This is because this long-chained polymeric molecule easily interacts with hydroxyl groups on the surface and the metal ions at a molecular level. This interaction reduces surface tension, controlling the rate at which the sol particles grow. He et al. (2020) synthesized $ZnWO_4$ nanoparticles via variation of different concentrations of ethylene glycol; it was observed that the size of the synthesized nanoparticles decreased as the concentration of the ethylene glycol increased, further proving that ethylene glycol plays a huge part in size manipulation during synthesis as its presence inhibited the growth of the $ZnWO_4$ nanoparticles. The sizes

were reduced from 100 nm for $ZnWO_4$.EG0 to 5 nm for $ZnWO_4$.EG75. Neto et al. (2020) also found out that the size of $ZnWO_4$ nanoparticles obtained was greatly influenced by the increasing hydrothermal treatment time by increasing the time from 5 to 120 min; the size was greatly influenced by the $ZnWO_4$ nanoparticles increased from 39.83 – 217.18 Å. Using ethylene glycol and PEG as surfactants have led to the production of $ZnWO_4$ nanoparticles having smaller sizes than the nanoparticles synthesized using SDBS as a surfactant; the range was 25–30 nm (Mosleh and Teheringat, 2016). Mehdi et al. (2015) proposed that the size of $ZnWO_4$ nanoparticles produced was strongly affected by experimental factors such as Zn^{2+} and WO_4^{2-} concentration (M), Zn^{2+} feed flow rate, and temperature. The authors observed that a change in the reaction conditions determined the diameter of the product, and the size of nanoparticles synthesized at the optimal conditions was 30nm. Unfortunately, it was discovered that the flow rate of Zn^{2+} ions did not affect the diameter of the $ZnWO_4$ nanoparticles. TEM images obtained from Garadkar et al. (2013) showed how the $ZnWO_4$ nanoparticles have a uniform and narrow size distribution, just like Paliki et al. (2016) of between 5–7 nm; in this case, the nanoparticles were between 10-15 nm. Using a logarithmic scale, the particle size distribution was presented and determined to be 26 μm. The scale is in micrometres means that the $ZnWO_4$ nanoparticles obtained are mesoporous, making them the most suitable for enzyme immobilization. The research was carried out by Sivaganesh et al. (2020) using HMTA as a surfactant that had the smallest size at 14 nm; however, when PVP was used, the size of the nanoparticles was 30 nm, and when SDS was used, the size was 31 nm, however without the addition of any surfactants, the size of 16 nm was obtained. Furthermore, the size of the $ZnWO_4$ nanoparticles depended on the critical micelles concentration (CMC), but this is only true in the case of the nanoparticles obtained using SDS as a surfactant. This is solely because HMTA and PVP acted as surface capping agents and controlled the size of the nanoparticles during nucleation. During research by Jeong et al. (2020), it was established that the size of the particles differed in the temperature of fabrication as scintillator materials changed; nanoparticles fabricated at 700 °C had an average size of 176.4 nm those fabricated at 800 °C had an average size of 626.7 nm, and lastly, the nanoparticles fabricated at 900 °C had an average size of 2.127 μm. This scenario was previously explained by Yang et al. (2009). Geetha et al. (2021a) varied the volume of solvent (distilled water) used to dissolve the precursors when synthesizing $ZnWO_4$ nanoparticles between 30 mL, 50 mL, 70 mL, and lastly, 90 mL. The diffusion distance for the growing species decreases as the solvent volume decreases. This was owing to a greater number of growth species being available in the reaction medium, resulting in a higher growth rate due to increased transfer and an increase in the crystallite size of the nanoparticles. When the amount of solvent decreases, diffusion distance increases due to a reduction in the concentration of growth species. This lowers the growth rate since the mass transfer is lower (Dehsari et al., 2017). In the end, even the FE-SEM images obtained further proved that the morphology of the nanoparticles obtained using 30 mL (lowest amount) as the volume of the starting solution yielded hexagonal nanoparticles, while the nanoparticles obtained when 90 mL (highest amount) was used as the volume of the starting solution yielded densely packed nanoparticles.

Another critical property frequently being checked is the shape of nanoparticles. Some researchers observed that sometimes $ZnWO_4$ nanoparticles synthesized had a pearl necklace-like shape with hollow structures; this was observed from the SEM and TEM analysis (Hao et al., 2017). The $ZnWO_4$ nanoparticles synthesized by Mehdi et al., (2015) at optimal conditions of 0.1 M of Zn^{2+} and WO_4^{2-} ion concentration (M), 2.5 mL/min Zn^{2+} feed flow rate (mL/min) to the WO_4^{2-} solution and 60 °C temperature were spherical-shaped. TEM images from the research carried out by Yan et al. (2013) show that the nanoparticles obtained had a nanorod morphology. Using ethylene glycol, $ZnWO_4$ nanoparticles were synthesized at pH 10 by Garadkar et al. (2013), and the particles were well-dispersed spherical nanoparticles. It was even reported by Faka et al. (2021) that an increase in temperature leads to even more spherical-shaped nanoparticles. PEG concentration also played a prominent role in determining the shape of formed $ZnWO_4$ nanoparticles. It has been observed by Geetha et al. (2019) using the presented SEM images that $ZnWO_4$ nanoparticles synthesized with PEG had a spherical morphology; however, these new $ZnWO_4$ nanoparticles had a more uniform and homogenous particle size distribution. The polymeric surfactant PEG caused a change in the morphology of the formed nanoparticles. The addition of PEG into the mixture led to the formation of a complex by Zn^{2+} ions with PEG, resulting in the capping of the $ZnWO_4$ nanoparticles at the nucleation stage. This researcher concluded that the presence of PEG in a reaction mixture led to the formation of stabilized $ZnWO_4$ nanoparticles incapable of agglomerating (Cholan et al., 2014). Exploration into photocatalysis has shown how UV-light, Visible light, and solar irradiation can be utilized effectively to reduce environmental pollution Zhang et al. (2014a,b). Electron hole pairs are formed when photon energy greater than the semiconductor's bandgap is used to illuminate the semiconductor, resulting in the formation of electron-hole pairs, OH radicals are typically formed when generated electrons and holes react with H_2O and molecular oxygen on the crystal's surface.

4. Photocatalytic applications of undoped and doped $ZnWO_4$ nanoparticles

4.1. Photocatalyst for wastewater treatment

The degradation of harmful and toxic pollutants in our water bodies has become a concern worldwide. Photocatalysis has proven to be very effective at degrading organic contaminants due to its ability to use the sun, solar, and even UV energy to trigger photocatalysis (Raizada et al., 2017b). This process generates e^-/h^+ pairs participating in oxidation/reduction reactions with the organic contaminants, causing their degradation. As far as the field of wastewater treatment is concerned, most research has focused on applying $ZnWO_4$ nanoparticles to remove organic and inorganic dyes. In some cases, $ZnWO_4$ nanoparticles have been used to remove bacteria from water samples (He et al., 2020; Pavithra et al., 2021).

The degradation of RhB was evaluated using $ZnWO_4$ nanorods doped synthesized with different amounts of B^{3+}. The adsorption efficiency of B doped $ZnWO_4$ in the dark was investigated, and it was discovered that the efficiency increased as the B content increased, which directly increased the surface area of the composite samples. The photocatalytic activity of the B-doped $ZnWO_4$ nanorods was higher than the pure $ZnWO_4$ nanorods when exposed to UV light. Doping $ZnWO_4$ decreased the average crystallite size, increasing the nanorods' specific surface area (47.20 m^2/g). This reduction in crystallite size can reduce charge transfer distance, aiding in the separation of photogenerated electron holes. B doping has also resulted in a more efficient separation of photogenerated electron-hole pairs in $ZnWO_4$ nanorods, accounting for 96.13 %. Finally, the maximum degradation of RhB by (2.42 wt.%) B/$ZnWO_4$ was observed. The degradation of other dyes such as acid orange II and methyl orange was also investigated. In both cases, (2.42 wt%) B/$ZnWO_4$ had the highest degradation percentage, followed by pure $ZnWO_4$ (Liu et al., 2017).

During most dye degradation processes, excited electrons in some dyes could not transfer to the photocatalyst's conduction band because the level of the excited states in some dyes remains lower than the photocatalyst's conduction band, where the photosensitized process was hampered. Qureshi et al. (2019) synthesized graphene oxide (GO) decorated $ZnWO_4$ (GO-$ZnWO_4$) nanocomposite for the degradation of Cetirizine dihydrochloride (C–HCl). Using RSM, in this case, C–HCl was adsorbed over the surface of the GO-$ZnWO_4$ composite. Superoxide and peroxide radicals were also produced as reactive oxygen species (ROS) when photo-trapped electrons react with surface adsorbed oxygen. These photo-trapped electrons move from the conduction band, are trapped over the graphene network, and channeled to photo-excited electrons. The hydroxyl radicals were generated and responsible for C–HCl, CO_2,

and H_2O oxidative degradation. The optimum conditions to achieve 89 % degradation rates were as follows, pH = 7, C–HCl concentration = 10 mg/L, catalyst dose = 425 mg/L, and the irradiation time was 120 min. This is in line with the predicted degradation through the RSM model. During photolysis, a redox process is initiated over the surface of the catalyst as a result of the electron holes generated by light absorption, and another set of reactive species in the form of peroxide and superoxide radicals were formed as a result of the redox process (Qureshi et al., 2019; Zhang et al., 2014a,b).

Sethi et al. (2019) found CdS doped on $ZnWO_4$ photocatalysts effective for the degradation of RhD under solar irradiation than $ZnWO_4$ alone, and the complete degradation of RhB took place when CZW-4 (synthesized using 20 mol% of $Cd(NO_3)_2.4H_2O$ was utilized, other samples synthesized included CZW-1, CZW-2 and CZW-3 having 5, 10 and 15 mol% $Cd(NO_3)_2.4H_2O$, the whole degradation process took place in 50 min. Generally, photocatalytic activity depends on phase structure, optical absorption, and charge carrier separation efficiency (Sethi et al., 2019; Xu and Qu, 2014).

Geetha et al. (2021b) observed a reduction in the percentage degradation of MB from 87% > 85 % > 78 % for $ZnWO_4$ nanoparticles calcined at 300 °C, 400 °C, and 500 °C were applied, respectively, as depicted in Figure 3. An experiment was conducted in the absence of $ZnWO_4$ where 0 % degradation was observed, proving that $ZnWO_4$ nanoparticles are essential for wastewater treatment. As seen in Figure 3, an increase in the treatment time increased the percentage of MB degraded. It was further reported that the photocatalytic activity of $ZnWO_4$ nanoparticles was governed by two major parameters: the crystallite/particle size between 30-65 nm and the surface area. This means that $ZnWO_4$ nanoparticles with a large surface area and small crystallite size were very effective in degrading MB pollutants. The observed trend was caused by more surface defects responsible for the absorption molecules that produced photogenerated carriers and charge separation when exposed to UV light. Based on nanocrystals' larger crystallite size and agglomeration at higher temperatures, samples calcined at 500 °C had lower photocatalytic activity.

$ZnWO_4$ has unique magnetic, catalytic and luminescent properties and has, over the years, been utilized as a very efficient photocatalytic material capable of producing hydrogen and mineralizing organic pollutants (Luo et al., 2018; Yesuraj and Suthanthiraraj, 2019). In the study of Carvalho et al. (2019), the XRD results revealed that the heterostructures made up of 3Zn:1ZnW and 1Zn; 1ZnW (1 and 3 represented the mole ratios) exhibited higher photodegradation efficiency (80 %) of methylene blue dye after 180 min compared to pure ZnO and $ZnWO_4$. On the other hand, caffeine, an alkaloid, was almost entirely oxidized by the heterostructures after 180 min Figure 4 describes the photogenerated electron in the conduction band of ZnO (−0.36 eV) and $ZnWO_4$ (−0.14 eV). It was discovered that photogenerated holes in the valence band of $ZnWO_4$ (+3.66 eV) migrate to the valence band of ZnO (+2.84 eV), improving the heterostructure's effective spatial charge separation. The hetero-structures degraded the hypertensive drug Amiloride by 85 % after only 60 min, unlike pure ZnO and $ZnWO_4$. The heterostructures were also used to degrade organic pollutants in the gas phase. With nearly 100 % ethylene degradation after 180 min in both cases, the efficiency of the heterostructures was much higher than that of pure ZnO and $ZnWO_4$. Gas chromatography analysis proved no formation of secondary pollutants. This suggests that ethylene was entirely mineralized into CO_2 and H_2O and the concentration of CO_2 generated increased as ethylene concentration decreased. This heterostructure ZnO:$ZnWO_4$ showed higher photocatalytic activity against water-soluble contaminants such as caffeine, MB, and Amiloride and gaseous pollutants such as ethylene. The interaction between these two helped improve photo-activity and stability, which enabled the degradation of environmental pollutants in different phases (Carvalho et al., 2019).

Zhao et al. (2020) investigated the photo-degradation efficiency of $ZnWO_4$ nanoparticles and discovered that $ZnWO_4$ can be used for efficient wastewater treatment and the degradation of organic pollutants. Vacuum filtration was used to create composite photocatalytic membranes of zinc tungstate nanoparticles, nickel-aluminium-layered double hydroxides, and polyvinylidene fluoride ($ZnWO_4$/NiAl-LDH/PVDF). MB was photodegraded using as-synthesized NiAl-LDH, $ZnWO_4$, and ZWLDH composites. It was observed that NiAl-LDH had the lowest degradation performance with only 24.22%, NiAl-LDH combined with $ZnWO_4$ increased the photocatalytic degradation with ZWLDH-20 (Having 20 mg of the NiAl-LDH onto $ZnWO_4$) achieved 93.97 % degradation rate. The degradation efficiency MB by the various samples synthesized varied from 24.73 % for the commercial P25, 67.88 % for the NiAl-LDH, 73.11

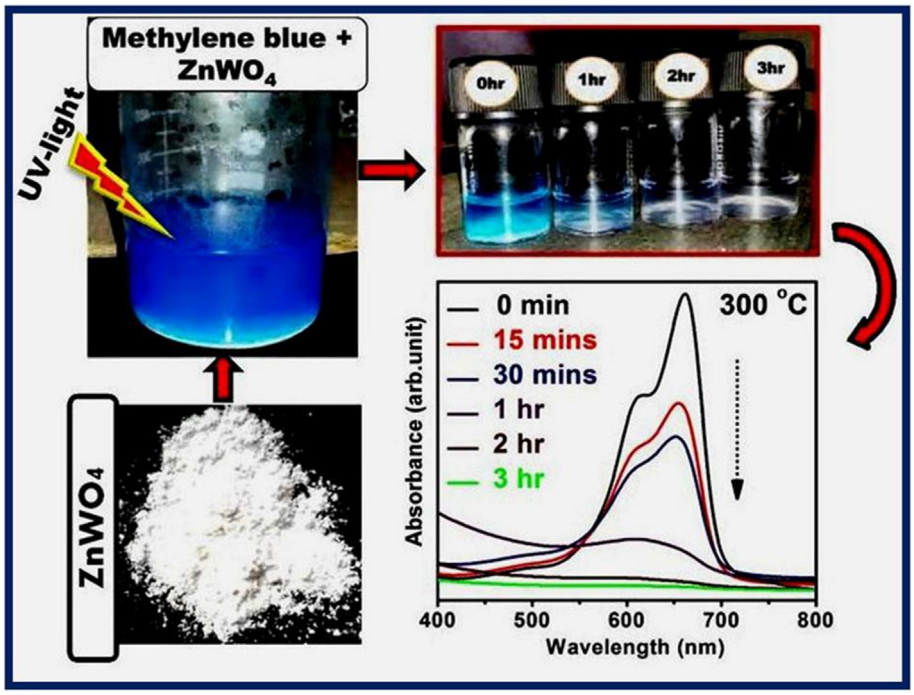

Figure 3. Water treatment pathway of MB and $ZnWO_4$ (Geetha et al., 2021b).

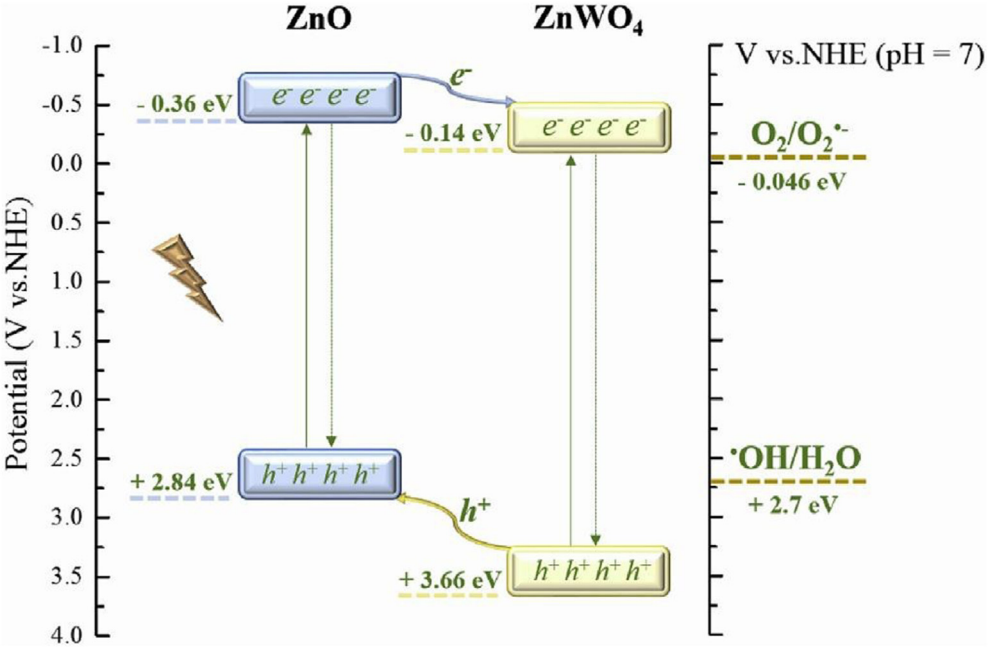

Figure 4. The charge-transfer process of ZnO and $ZnWO_4$ (Carvalho et al., 2019).

% for pure $ZnWO_4$, 86.55 % for ZWLDH-40, 84.27 % for ZWLDH-60, 80.55 % forZWLDH-80 and 76.74% for ZWLDH-100. The authors established that $ZnWO_4$ can be used to degrade MB; however, its performance can be enhanced by combination with NiAl-LDH. The most suitable composite was obtained using 20 mg of NiAl-LDH with $ZnWO_4$. Furthermore, the permeability behaviour of the samples was examined where the pressure within the system was raised from 0.1-0.5 bar. It was found that the sample labelled ZWLDH-20-PVDF2 having 20 mg of NiAl-LDH loaded with double hydroxides/polyvinylidene fluoride composite membranes had the best degradation potential when compared with other samples such as commercial P25, NiAl-LDH, $ZnWO_4$, ZWLDH-100, ZWLDH-80, ZWLDH-60, and ZWLDH-40 composites. During this study, some trapping agents were obtained for application in the degradation system. 1,4-benzoquinone (BQ), ethylenediaminetetraacetate (Na_2-EDTA) as well as isopropanol (IPA) were applied to the system to trap $\cdot O^{2-}$, h^+ as well as ·OH respectively. After adding BQ and IPA into the system, the efficiency of ZWLDH-20 at the degradation of MB reduced significantly under visible light; this shows that trap $\cdot O^{2-}$ and ·OH play an essential role in degradation.

Nanoparticles synthesized by He et al. (2020) were evaluated by a bacterial inhibition zone test using the probes *Bacillus subtilis* and *Vibrio alginolyticus*. It was now observed that when $ZnWO_4$/ethylene glycol (EG) (0 ml of EG) nanoparticles were used provided an unsatisfactory bacteriostatic effect from the test results having an inhibition zone diameter of 5.3 mm. The nanoparticles synthesized with 50 mL EG were labelled $ZnWO_4$-EG50 and had a better inhibition zone area of 6.6 mm. This research showed how an increase in EG led to better inhibition as ZnWO4-EG62.5 and ZnWO4-EG75 with 62.5 and 70 mL had even better inhibition zone areas of 8.6 mm and 9.3 mm, respectively, meaning a minimal inhibition was covered in the case of $ZnWO_4$-EGO. Since $ZnWO_4$-EGO is $ZnWO_4$, it is safe to say that pure $ZnWO_4$ nanoparticles can exhibit some bacterial activity; however, the presence of EG will make it much more effective.

Reddy et al. (2020) investigated the degradation of tetracycline (TC) using Z-scheme binary 1D $ZnWO_4$ nanorods decorated with 2D $NiFe_2O_4$ nanoplates. Pure $ZnWO_4$ was synthesized along with $NiFe_2O_4$, NFZW-10, NFZW-20, and NFZW-30, with the last four having different amounts of $NiFe_2O_4$ at 0, 10, 20 30 mg of $ZnWO_4$ respectively. In the absence of light, no degradation was noticed. To catalyze the process, pure $ZnWO_4$ (bandgap, 3.492 eV) and $NiFe_2O_4$ (bandgap, 1.707 eV) were used, after which 37 % and 43 % degradation were observed. Similar nanocomposites reported by Koutavarapu et al. (2022) were used for the photocatalytic degradation of Cr(VI), tetracycline, and methylene blue. According to Reddy et al. (2020), the respective valence and conduction bands of $ZnWO_4$ and $NiFe_2O_4$ were +3.836, +0.344 eV, and +1.009 and -0.698 eV, as established from the diagram shown in Figure 5. The photogenerated charge carriers migrate to the CB of $NiFe_2O_4$, and VB of $ZnWO_4$, producing OH radicals and h^+ radicals at the CB of $ZnWO_4$ and VB of $NiFe_2O_4$. The recombination of electron-hole pairs was reduced, leading to increased catalytic activity. Atla and Oh (2021) investigated the charge-transfer pathway for removing tetracycline antibiotics under solar light and followed the type-II heterostructure mechanism. It can be concluded that the yield of type-II heterostructure due to the coupling of ZnO with other semiconductors increases the spatial separation of the photogeneration charge carriers and the electron-hole pair. Degradation of TC by NFZW-10 (bandgap, 1.845 eV) was up to 87 %; that of NFZW-20 (bandgap, 1.784 eV) as high as 98 %, and lastly, NFZW-30 (bandgap, 1.829 eV) was much lower at 75 % for 105 min, under solar irradiation, this mechanism for this process can be seen in Figure 5. This study showed that the coupling of $ZnWO_4$ with $NiFe_2O_4$ using 30 g of $ZnWO_4$ and 100 g of $NiFe_2O_4$ formed an efficient photocatalyst for the degradation of tetracycline which was done in the presence of solar light. It was also noticed that coupling $NiFe_2O_4$ with large amounts of $ZnWO_4$ decreased its catalytic activity because of the surface coverage of $NiFe_2O_4$/$ZnWO_4$ composite by $ZnWO_4$. Radical trapping experiments were also carried out, in which case; Triethanolamine (TEA), Benzoquinone (BQ), and Isopropyl alcohol (IPA) were used to quench the active species for the hole (h^+), superoxide ($\cdot O_2^-$) as well as hydroxyl ($\cdot OH$) radicals. No degradation occurred in the absence of the catalysts; however, upon the addition, 35 % of RhB degraded in the case of $ZnWO_4$ while 44 % RhB was degraded by $NiFe_2O_4$, 84 % of the RhB dye was degraded by NFZW-10, 98 % by NFZW-20 and 77 % by NFZW-30. Again, NFZW-20 exhibited the highest degradation efficiency compared to the others. This further showed that an increase in the amount of $ZnWO_4$ above 20 mg will only decrease the catalytic efficiency of the sample. Several types of research have been done to further show the possible applications of $ZnWO_4$ in wastewater treatment, as seen in Table 4.

$ZnWO_4$ has been applied for the degradation of contaminants over the decade, where it was observed that the parameters to be varied for each

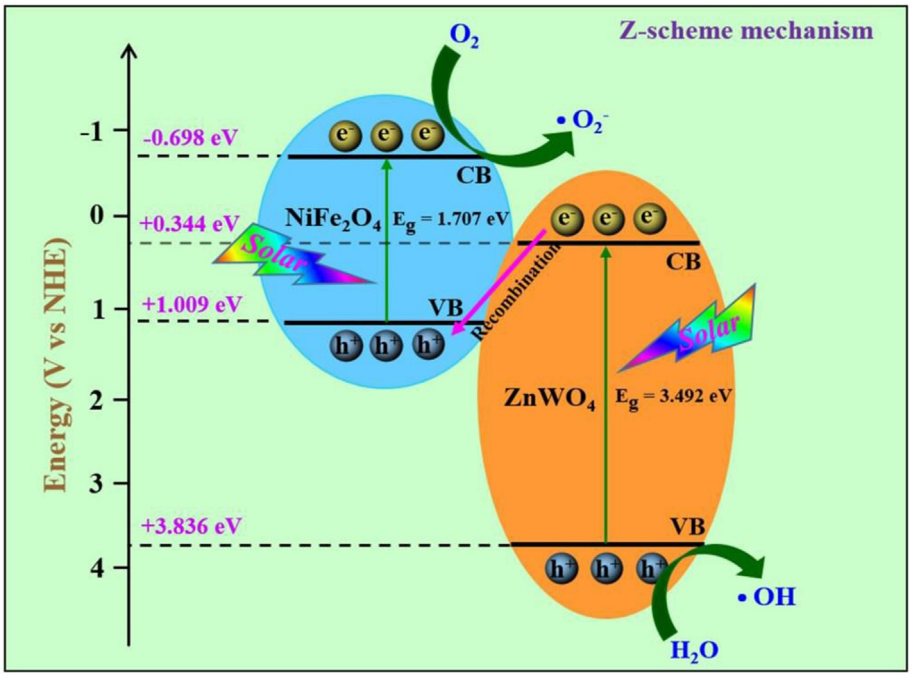

Figure 5. The direct Z-scheme photocatalytic mechanism of $NiFe_2O_4/ZnWO_4$ nanocomposites (Reddy et al., 2020).

contaminant. It was also observed that only doped $ZnWO_4$ was active under sunlight. From the synthesis stage, the amount of solvent used determined the efficiency of the final product, as it was observed that the higher the volume of solvent used, the lower the efficiency as a result of the dilution effect, which results in a decrease in the amount of reacting molecules.

4.2. $ZnWO_4$ photocatalyst as antimicrobial agents

According to the World Health Organization (WHO), the leading causes of death are infections and parasitic diseases; globally, approximately 2 million deaths occur from bacterial infections alone, as one-third of the population is infected with bacterial pathogens (Haque

Table 4. Recent research where $ZnWO_4$ was utilized as a photocatalyst for wastewater treatment.

Pollutant Degraded	Precursors and reaction conditions	Characterization techniques	Research findings	References
Caramine Indigo (CI) and Crystal Violet (CV)	$Na_2WO_4.2H_2O$, $Zn(NO_3)_2.4H_2O$, EG. pH = 9.5	XRD, FTIR and UV-VIS	There was no change in the absence of the catalyst; however, when 1g of the catalyst was used, complete degradation of the pollutants occurred after 150 and 180 min for CI and CV, respectively, all under visible light irradiation.	Paliki et al. (2018)
Meloxican (M2X) ($Ag_2O/ZnWO_4$)	$Na_2WO_4.2H_2O$ and $Zn(NO_3)_2.4H_2O$. Dried at 453 K for 24 h.	XRD, SEM, XPS, and BET	The best sonocatalytic decomposition of M2X was achieved when 0.5 g/L of the $Ag_2O/ZnWO_4$ composite was used for 120 min at a power of 200W ultrasonic radiation and a concentration of 10.0 g/L M2X solution.	Wang et al. (2021)
Methylene blue (MB) dye	Na_2WO_4 and $ZnCl_2$. Dried at 80 °C for 6 h.	XRD, FE-SEM, PL and UV-VIS	This study synthesized $ZnWO_4$ nanoparticles using different volumes of solvents. The highest degradation efficiency was observed using the nanoparticles obtained with just 30ml of the solvent at 81%. This results from more active sites, species, and nanopores on the surface of the nanoparticles. When $ZnWO_4$ nanoparticles synthesized using 90ml of solvent were applied, the efficiency dropped to 94% as a result of the dilution effect as well as a decrease in the number of reaction molecules which are not enough to break down MB.	Geetha et al. (2021a)
Rhodamine blue (RhB)	ZnO, WO_3 and Li_2CO_3	XRD, FTIR, UV-DRS	$Zn_{0.9}WO_4$:0.1Li+ was the most efficient for the degradation of RhB under UV irradiation compared to the other three phosphors $Zn_{1-x}WO_4$:xLi^+ with x = 0, 0.02 and 0.05 at 32.1%, 59.8% and 76.4% respectively after exactly 120 min of irradiation. The three doped phosphors have a much higher photocatalytic activity than pure $ZnWO_4$ phosphors.	Xiong et al. (2018)
Rhodamine blue (RhB)	ZnO, WO_3 and TiO_2	XRD, UV-VIS, PL and XPS	0.01Ti^{4+} doped $ZnWO_4$ degraded up to 97% of RhB in 120 min, while pure $ZnWO_4$ showed a slightly lower photocatalytic activity with a degradation efficiency of only 87% under UV irradiation, 0.02g of catalyst was used, and the concentration of the organic pollutant was 4×10^{-5} mol/L.	
Methyl orange (MO)	$Na_2WO_4.2H_2O$, $Zn(NO_3)_2.4H_2O$ and $Na_2HPO_4.12H_2O$	XRD, SEM, and TEM	Pure Ag_3PO_4 degraded 54% of Methyl orange after 55 min, ZA-4, ZA-3, ZA-2, and ZA-1 with 0.04, 0.03, 0.02 and 0.01 g of $ZnWO_4$ degraded 72%, 79%, 95% and 93% MO respectively. This means that $ZnWO_4/Ag_3PO_4$ has a higher degradation efficiency than the two in their pure forms. An increase in the amount of $ZnWO_4$ on Ag_3PO_4 (beyond 0.01g) resulted in a lowering photocatalytic activity of the composite material. This is because the presence of more $ZnWO_4$ on the surface of Ag_3PO_4 ended up taking the place of the active catalytic sites of Ag_3PO_4 hence why the decomposition of MO did not increase as the amount of $ZnWO_4$ increased.	Zhang et al. (2017a,b)

et al., 2014; WHO, 2021). An antimicrobial agent is a natural or synthetic substance capable of killing or inhibiting the growth of microorganisms such as bacteria, algae, and even fungi. Although microorganisms frequently develop antibiotic resistance, most resistance mechanisms are irrelevant. Nanoparticles work differently because nanoparticles have direct contact with the cell walls of the microorganisms. He et al. (2020) established that $ZnWO_4$ favours the release of the antibacterial substance, $Zn^{2+,}$ which is responsible for inhibiting *Bacillus subtilis* and *Vibrio*. Similar observations were reported by Ahmed et al. (2022), that used graphene oxide/$ZnWO_4$ against the bacterium. These nanomaterials could serve as media and carriers for antibiotics, helping to raise serum levels of antibiotics while also protecting the drugs from bacterial resistance. In the process, specific parameters are checked, including the shape, surface area, particle size, and surface curvature, which affect the antibacterial activity of the nanoparticles. Thus, the $ZnWO_4$ could serve as a long-lasting antimicrobial agent that will destroy microorganisms due to the generation of hydroxyl radicals and superoxide radicals when exposed to solar radiation or ultraviolet light.

5. Shortcomings of $ZnWO_4$ nanoparticles

Exploration into photocatalysis has shown how UV-light, Visible light, and solar irradiation can be utilized effectively to reduce environmental pollution light (Zhang et al., 2014a,b). Electron hole pairs are formed when photon energy greater than the band gap of the semiconductor is used to illuminate the semiconductor, which results in the formation of electron-hole pairs, OH radicals are typically formed when generated electrons and holes react with H_2O and molecular oxygen on the crystal's surface. Photocatalysis has been an outstanding technology due to its low energy consumption, operational safety, high efficiency, and role in environmental pollution control (Yu et al., 2016). Among the challenges associated with $ZnWO_4$ is the occurrence of low absorption at wavelengths near the UV-visible region, and this is due to their electronic configuration, which has a high electron/hole pair recombination rate (Neto et al., 2020). $ZnWO_4$ nanoparticles have demonstrated excellent photocatalytic activities in the field of wastewater treatment over the years; however, $ZnWO_4$ nanoparticles have low photocatalytic activity in the ultraviolent region due to the wide band gap of $ZnWO_4$ nanoparticles, which is between 3.7–5.8 eV, making practical applications difficult (He et al., 2020). A low surface area for adsorbing pollutants, large particle sizes to increase the electron-hole migration distance, and low crystallinity to enhance the electron-hole recombination rate could all contribute to the photocatalyst's low activity.

Pure $ZnWO_4$ nanoparticles do not always have good crystallinity and, in most cases, have irregular morphologies (Sivaganesh et al., 2020). Raizada et al. (2017a) discovered that doping $ZnWO_4$ nanoparticles with metal or nonmetal impurities can reduce the problem of high electron-hole recombination and increase the absorption threshold in the visible region. There has also been a report on one more hindering factor: its difficulty of separation, usually from a reaction solution. However, these are some issues faced when using bare metal oxides. Most studies have applied these bare metal oxides in aqueous media, but unfortunately, metal oxides do not work well in aqueous phases due to their low adsorption. However, photogenerated electron-hole pairs recombined quickly and have a weak sensitivity to visible light, making them impractical to use as photocatalysts. Many attempts have been made to minimize the recombination rate of photogenerated electron-hole pairs and increase the visible light photoresponse (Zhang et al., 2017a,b).

6. Strategies to solve the shortcoming and new perspectives of $ZnWO_4$ nanoparticles

Doping has long been used to improve nanoparticles' optical, electrical, and biological activities. Using rare-earth metals, dopant impurities such as Mn^{2+}, Co^{2+}, and transition elements alter the electronic structure and the host material's ability to become modulated. The structure of dopants and magnetic and electrical properties can be tuned by a method known as co-doping. There are two types of dopants: positive p-type dopants and negative n-type dopants. The former aids conduction by accepting electrons when added to the atomic lattice of the semiconductor; the latter allows positive holes to form quickly because it can host electrons from the conduction band. The n-type dopants, on the other hand, have more valence electrons with energies very close to the conduction band and act as electron donors. The valency of the n-type dopants is easily excited to the conduction band when they get incorporated into the semiconductor's atomic lattice (Chen et al., 2013; Phung et al., 2017).

Co-doping with the nonmetals nitrogen and carbon has proven effective at improving the efficiency of $ZnWO_4$ in the degradation of organic pollutants, as presented by Chen et al. (2013). One disadvantage of using $ZnWO_4$ is that it can only be activated under visible light. However, doping has proven effective at making $ZnWO_4$ active under visible light (Chen et al., 2013). Chitosan and other polymers such as polyethylene glycol (PEG) have also been used to dope nanomaterials, increasing antimicrobial efficiency against *B. subtilis*, *E. coli,* and *S. aureus*. This phenomenon provides an easy way in which the properties of nanomaterials can be tuned without affecting the high surface area of the material. Doping generally leads to the expansion or narrowing of the band gap of a nanomaterial due to a shift in the E_c positioning. This narrowing makes it possible for doped nanomaterials to be effective under visible light. Under visible light, this generates reactive oxygen species (ROS). Changes in lattice properties or, more likely, dopants acting as electron traps and inhibiting charge recombination are responsible for this. This could also be due to the intermediate energy level between the valence and conducting bands. Band bending as a result of doping is experienced in the case of doped nanomaterials, which enables the material to be photoactive under visible light, while its undoped version is only photoactive under UV light. This is possible due to the change in lattice parameters or when dopants prevent charge recombination because they act as electron traps. This phenomenon also results in an intermediate energy level between the valence and conducting bands, which may explain why ROS are produced when exposed to visible light (Lounis et al., 2014). However, it has been observed that besides doping, even the technique used to synthesize nanoparticles can determine the nature of the final nanomaterial as these processes can control the imperfections in crystalline nanoparticles, which can alter the band structure of the nanoparticles. The size and shape specific to metal oxide nanoparticles (MONPs), temperature, type of precursors, gas pressure, and other parameters can determine the formation defects of nanoparticles (Lounis et al., 2014; Schimpf et al., 2014). Nanoparticles can be doped with transition metals, noble metals, nonmetals, and semiconductors (Dutta and Raval, 2018). Over the past decades, doped metal nanoparticles have received much attention because they have interesting properties and promising applications (Yao et al., 2015).

Because the Fermi level of $ZnWO_4$ is less positive than that of the noble metal, doping it with noble metals can aid in rapidly separating photogenerated charges via the Schottky barrier. Doping $ZnWO_4$ with ions such as chlorine has enhanced the nanomaterial's photocatalytic activity because the atoms being doped act as electron traps, improving photogenerated charge separation. When $ZnWO_4$ is combined with materials such as graphene and C_3N_4, which have a π-π conjugated structure, the combination of photogenerated carriers is inhibited; this occurs due to the particular conductivity of the conjugated material. Combining $ZnWO_4$ with semiconductors such as BiOBr has provided a better route to effectively facilitate the charge's transition. This can significantly improve nanomaterials' photocatalytic performance (Tian et al., 2018). One of the primary reasons for nanomaterial doping is increased surface area, resulting in materials with short charge carrier diffusion lengths and abundant reaction sites. To broaden the absorption range, polymeric or molecular absorbers are surface sensitized with semiconductor materials (Dutta and Raval, 2018). Metal/nonmetal doping counters the recombination problem by enhancing the charge separation between

electrons and holes; these dopants trap electrons and accelerate the photocatalytic system by reducing the electron-hole recombination problem. Nonmetal doping of $ZnWO_4$ affects the crystallization and structural properties of the nanoparticles, which will, in turn, lead to the modification of the photocatalytic activity of the $ZnWO_4$ nanomaterials as the recombination of photogenerated charge carriers is lowered, this helps to improve light absorption. Nonmetal doping can help make the nanoparticles have better photoelectronic and environmental applications. An example of a nonmetal that can be used for doping is sulphur. There is a large electro-negativity between sulphur and oxygen, so doping with sulfur can help improve the structural and optical properties of the nanoparticles; since S^{2-} is larger than O^{2-}, doping with sulfur will make it substitute oxygen which then affects the lattice constant responsible for the electrical and optical properties being varied (Kumari et al., 2019).

Compared to monodoping, co-doping donates more electrons to the molecule, modifying its electronic structure even more. Although different metal groups such as alkali metals, alkali earth metals, transition metals, and even rare earth metals can be used, the difference in valence states causes each metal to donate a different number of electrons to the molecule. As a result, the amount of charges transferred to each molecule is determined by the dopant species. When metal dopants enter the molecular crystal, they settle in intralayer holes rather than the region between two layers. The stability of the doped nanomaterial is improved when the π electrons interact with the dopant in a hole (Yan et al., 2019). Co-doping, in general, has led to a decrease in the ionization energy of donors and acceptors, which then leads to an increase in the activation energy, even if the carrier mobility is increased (Zhang et al., 2016). Doping semiconductors with nonmetals are beneficial due to the mixing of the nonmetals' P orbitals with the semiconductor's 2p orbital, which helps reduce the band gap energy of the semiconductor. Doping the semiconductor with transition metal ions could shift its optical absorption edge from the UV to the visible light range. One disadvantage of metal doping is its low quantum efficiency and thermal instability. Co-doping with two nonmetals, metal and nonmetal, and two metals reduces this problem (Phung et al., 2017). The formation goes from tri-doped > co-doped > mono-doped > pure semiconductor. When Phung et al. (2017) synthesized and analyzed the effects of mono-doping, co-doping, and tri-doping on TiO_2, the bandgap energies were also reduced significantly by forming N_{2p} bands close to the top of the valence band, which increased visible photocatalytic activity.

Yadev et al. (2018) studied tri-doped $ZnWO_4$ using Tm^{3+}, $Yb^{3+,}$ and Mg^{2+} phosphors; it has been reported that Mg^{2+} in co-doped phosphorus improves crystallinity as well as the intensity of the absorption bands, effectively doubling the phosphors' emission intensity. It also improved the crystallinity and the intensity of the absorption bands, doubling the phosphors' emission intensity. It also led to a decrease in the optical bandgap of the phosphors. It was observed that Tm^{3+}, $Yb^{3+,}$ and Mg^{2+} tri-doped $ZnWO_4$ phosphorus is applicable for temperature sensing, photonic devices, and even optical heaters (Yadav et al., 2018). It was also reported by that doping $ZnWO_4$ with Tm^{3+}, $Yb^{3+,}$ and Mg^{2+} can enhance the light-harvesting capability of $ZnWO_4$, which will then lead to the generation of more electron-hole pairs, it also decreases the recombination of photogenerated electron holes by acting as traps centres (Rao et al., 2019). Doping ions have improved the adsorption of photons and have even inhibited the recombination of electron-hole pairs (Rao et al., 2019).

Chen et al. (2013) proposed doping $ZnWO_4$ nanoparticles with carbon and nitrogen to improve photocatalytic efficiency under visible light. Because carbon has electron transport properties, the authors believe that carbon modification of $ZnWO_4$ photocatalysts could accelerate charge transfer from the photocatalyst to the liquid-solid interface with the organic pollutants. The authors employed pyrolysis of tripolycyanamide to generate C_3N_4 as a carbon and nitrogen source, respectively. XRD results showed strong and intense diffraction peaks, a sign of good crystallinity. The effect of loading of C_3N_4 on the efficiency of the $ZnWO_4$ photocatalyst was also investigated, and it was observed that the photocatalytic activity of the nanoparticles did not increase as the loading amount of C_3N_4, although it had some effect. It was also observed that shielding of active sites on the photocatalyst surface occurred by introducing a large percentage of C_3N_4. Despite blocking active sites, the $C_3N_4/ZnWO_4$ nanoparticles demonstrated higher photocatalytic activity in degrading RhB dye when exposed to visible light than pure $ZnWO_4$ nanoparticles.

Eu^{3+} and Tb^{3+} were doped separately onto the surface of the $ZnWO_4$ nanoparticles. During this study, the samples were characterized, and the results were compared. XRD patterns show no new phases formed due to the doping, and doping of the $ZnWO_4$ nanoparticles did not affect the crystallinity of the final product. Because Eu^{3+} has a higher ionic radius than Zn^{2+} at 0.095 nm for Eu^{3+} and 0.074 nm for Zn^{2+}, Eu^{3+} is located in the Zn^{2+} sites and not W^{6+} because Eu^{3+} has a larger ionic radius hence the difficulty of it to be found in W^{6+} active sites. Tb^{3+} also behaves the same way since its ionic radius is 0.092 nm. It was also observed during this research that doping of $ZnWO_4$ nanoparticles with Eu^{3+} and Tb^{3+} increased the radius of the nanoparticles significantly; this change was also attributed to the change in pH with the addition of $Eu(NO_3)_3.6H_2O$ for $ZnWO_4$:Eu^{3+} and $Tb^{3+}(NO_3)_3.6H_2O$ for $ZnWO_4$:Tb^{3+} (Li et al., 2013).

The coupling of $ZnWO_4$ nanoparticles with one or two semiconductors has become a promising strategy to increase the efficiency of the $ZnWO_4$ and other conventional metal oxide photocatalysts. In the case of solar irradiation, the propensity of e^-/h^+ recombination is minimized as $ZnWO_4$ nanoparticles are also doped with a halide or a metal ion; this whole process helps to tune the band gap of the nanoparticles. By reducing the $ZnWO_4$ nanoparticles to a nano-dimension, the surface area of the nanoparticles can be increased to promote quick interfacial charge transfer to the pollutants adsorbed onto the surface of the nanoparticles. The effects of transition metal doping were studied where TEM images showed that the average size of the $ZnWO_4$ nanoparticles decreased with doping; this same effect was noted by Su et al. (2012) while doping with Sn^{2+} for tunable optical and visible photocatalytic properties. In this case, with Cr^{3+}, Cu^{2+}, and Mn^{2+}, the dopant ions occupy the surface sites and decrease the coalescence of crystals, prohibiting particle growth. Photodegradation experiments were carried out using MB dye, and it was discovered that all of the doped nanoparticles outperformed the undoped nanoparticles in terms of photocatalytic performance. This was attributed to a decrease in the size of the nanoparticles, which increases surface area. The time taken for the degradation of MB was 150, 120, 90, and 75 min for $ZnWO_4$, $ZnWO_4$:Mn^{2+}, $ZnWO_4$:Cr^{2+}, and $ZnWO_4$:Cr^{3+} respectively, at 2 mol%. The process was done under visible light irradiation. It was noticed that $ZnWO_4$:Cr^{3+} with the lowest band gap at 2.72 eV was the most efficient when compared with the others $ZnWO_4$:Cr^{2+} at 3.08 eV, $ZnWO_4$:Mn^{2+} at 2.76 eV and lastly $ZnWO_4$ at 3.21 eV.

Dutta and Ravel (2018) prepared $ZnWO_4$ nanoparticles with a higher band gap at 3.21 eV and found that monodoping of $ZnWO_4$ nanoparticles with Cr^{3+}, $Cu^{2+,}$ and Mn^{2+} led to the formation of nanoparticles with a much lower band gap at 2.71 eV, 3.08 eV, and 2.76 eV respectively. It was noticed that undoped $ZnWO_4$ had lower catalytic performance and the longest time to degrade MB organic dye. However, when the time was reduced during the application of the doped nanoparticles, the lowest time was observed after doping the $ZnWO_4$ nanoparticles with Cr^{3+}, especially $ZnWO_4$:Cr^{3+}. Another researcher grew CdS on $ZnWO_4$ nanoparticles, where the XRD analysis confirmed the formation of the monoclinic and hexagonal phases of CdS. It was observed that an increase in the concentration of the CdS led to an increase in the intensity of the CdS peaks. HRTEM of CdS@$ZnWO_4$ shows a clear heterostructure formed due to the attachment of CdS onto the $ZnWO_4$ surface (Sethi et al., 2019).

Another process that has been used by researchers for the enhancement of $ZnWO_4$ nanoparticles is graphene hybridization. The photocatalytic activity of the $ZnWO_4$/graphene mixture increased as the proportion of graphene increased. Due to an excess of graphene in the photosystem, the optimum activity was observed when $ZnWO_4$/graphene reached 0.2 wt %. A further increase in graphene content above

the optimum resulted in a decrease in its photocatalytic activity. Furthermore, this study showed how with the controlled hybridization of graphene, the photocatalytic activity of UV light can be enhanced and visible light photocatalytic activity induced. This means a synergetic effect occurred between graphene and $ZnWO_4$ nanoparticles (Bai et al., 2012).

Sadiq and Bhat (2017a) synthesized $ZnWO_4$/RGO nanocomposites using the simple microwave irradiation method, and TEM images revealed rod-like nanoparticles on the surface of the RGO (reduced graphene oxide) sheets during characterization. This study utilized $ZnWO_4$/RGO for the photocatalytic degradation of MB and found that the $ZnWO_4$ nanoparticles containing RGO were more efficient for the degradation of MB than pure $ZnWO_4$ nanoparticles. Irrespective of the concentration of RGO for ZWRG-1% (1 % and 3 % solution of RGO as dopant), the photocatalytic activities of $ZnWO_4$ nanoparticles increased significantly. Beyond 3% RGO, the efficiency decreased because RGO covered the surface of the $ZnWO_4$ nanoparticles and, in the process, prevented the nanoparticles from absorption of light, hence reducing the activity. Under the same conditions, the degradation of methyl orange (MO), an anionic dye, and RhB, a cationic dye, was also studied, and it was noticed that the degradation of the cationic dyes was 82.85 % and 77.06 % for MB and RhB respectively, a much lower degradation for the anionic dye MO at 61.81 %. RGO provides a partially negatively charged surface; hence MO cannot be adsorbed efficiently on the catalyst's surface and the cationic dyes.

$ZnWO_4$ nanoparticles were doped with nitrogen to enhance the effectiveness of the nanoparticles for the degradation of MB. It was observed that the N-demethylation was the main mechanism that led to the degradation of MB as the use of N–$ZnWO_4$ results in N-demethylation and oxidative degradation. This study also observed that these synthesized nanoparticles adsorbed a reasonable amount (15 %) of dye even in the dark (photolysis). For this reason, it was also found that MB adsorption on the surface of N–$ZnWO_4$ was the primary reaction step even before photocatalysis. However, faster reaction rates were observed for the photocatalytic process than pure $ZnWO_4$ at 99.1 % after 120 min and 97.62 % after 240 min; it is still not strong enough to degrade the organic dye. It was also noticed that nitrogen only decreases the recombination of photogenerated e^-/h^+ pairs, which increases light harvest capabilities. Adding nitrogen into the system reduces the bandgap (Dutta and Raval 2018), increasing light adsorption in the visible region (Rahmani and Sedaghat, 2019).

Palladium (Pd) was used by Al-Amshany and Hussein (2018) to dope $ZnWO_4$ nanoparticles synthesized via the hydrothermal route, where XRD results showed a decrease in the $ZnWO_4$ diffraction peaks as the wt.% of Pd increased. Further analysis of the XRD results showed that the crystallite sizes changed upon adding Pd. It was noticed that an increase in the amount of Pd led to a decrease in the crystallite size. Photocatalysis was significantly affected by Pd loading, as 1.65 wt% increase of Pd from 0 led to an increase in the photocatalytic activity to 100 %. However, it was observed that an increase beyond 1.65 wt% resulted in low photocatalytic efficiency of the Pd doped nanoparticles. This study degraded atrazine completely by increasing the weight of Pd to 1.05 wt% from 0.5 – 1.0 g/L. Due to an increase in the active sites. Zhang et al. (2017a,b) synthesized $ZnWO_4/Ag_3PO_4$ semiconductor using the hydrothermal method for the photodecomposition of RhB dye. XRD results showed that the samples contained cubic Ag_3PO_4 and monoclinic crystals of $ZnWO_4$ (see Figure 5). The mechanism of doping of $ZnWO_4$ with Ag_3PO_4 and the eventual formation of hydroxyl radicals in sunlight is shown in Figure 6. $ZnWO_4$ was doped onto Ag_3PO_4 to form nanocomposites at different concentrations in this research work. As the ratio of $ZnWO_4$ in the catalyst increased, the particle size of Ag_3PO_4 decreased. Elemental mapping using EDS further proved the existence of the $ZnWO_4/AgPO_4$ composites. Photocatalytic studies revealed that a 4 % $ZnWO_4/AgPO_4$ composite was the most active, completely degrading the RhB dye under visible light irradiation in 8 min. The composite formed was made in other mole ratios besides 4 %, which were 0 %, 2 %, 6 % as well as 8 % $ZnWO_4/AgPO_4$. 4 % $ZnWO_4/AgPO_4$ was the most efficient, while 0 % $ZnWO_4/AgPO_4$ which is pure $AgPO_4$ was the least active. The bandgap energy of $AgPO_4$ (the least effective) was found to be 2.4 eV and 2.38 eV for 4 % $ZnWO_4/AgPO_4$ (most effective).

Some researchers went as far as increasing the number of dopants used by making it a ternary system, Marsooli et al. (2020) synthesized the ternary nanocomposite $Fe_3O_4/ZnWO_4/CeVO_4$, the binary nanocomposite $Fe_3O_4/ZnWO_4$ and Fe_3O_4 nanoparticles using the co-precipitation method with a sonochemical-assisted method and the results from all three were compared. It was observed from the XRD analysis that the crystallite size increases from 0.15, 36.3–58.7 nm for single, binary and ternary systems, respectively. Under UV light irradiation, this researcher also performed photocatalytic degradation of contaminants such as MB, MO, RhB, and Fenitrothion (FNT). In 120 min, $Fe_3O_4/ZnWO_4/CeVO_4$ had the highest MB degradation of 84 %. Finally, it was determined that the $Fe_3O_4/ZnWO_4/CeVO_4$ nanocomposite had the best photocatalytic activity at a molar ratio of 1:2:1 due to efficient electron-hole separation. This study was conducted in the presence of visible light. Hamrouni et al. (2015a,b) investigated the photocatalytic decomposition of 4-methoxybenzyl alcohol (4-MBA) to *p*-anisaldehyde (PAA) using binary and ternary SnO_2–ZnO–$ZnWO_4$ nanocomposites prepared using a sol-gel route. They revealed that the photo-efficiency of the mixed samples for the oxidation of 4-MBA to PAA was superior to $ZnWO_4$. All the nanocomposites were much more active when compared with the pure catalysts due to the contemporaneous presence of more than one semiconductor in a system, leading to a synergistic effect. Semiconductors possess different energy levels of their valence bands as well as conduction. In this case, the results of the electronic characterization have to be taken into consideration. In the absorption of UV radiation of Zn–$Sn_{0.05}$ and Zn-$ZW_{0.05}$, electrons move from the cathodic conduction band of ZnO to the anodic conduction band of SnO_2 and $ZnWO_4$, respectively. Thus, separation increases the charge carrier, improving the efficiency of the interfacial charge transfer onto the adsorbed molecules. Because the conduction bands of SnO_2 and $ZnWO_4$ are less cathodic than those of ZnO, the catalysts transferred photogenerated electrons to the molecular oxygen adsorbed on the surface of the mixed conductors. Holes transferred from the more anodic valence bands of SnO_2 or $ZnWO_4$ to the valence band of ZnO form hydroxyl radicals, which are responsible for the degradation of 4-nitrophenol. The authors attribute the binary samples enhanced photocatalytic activity to local heterojunctions between SnO_2 and $ZnWO_4$ or ZnO and $ZnWO_4$, resulting in the separation of photogenerated e^-/h^+ pairs. Table 5 presents

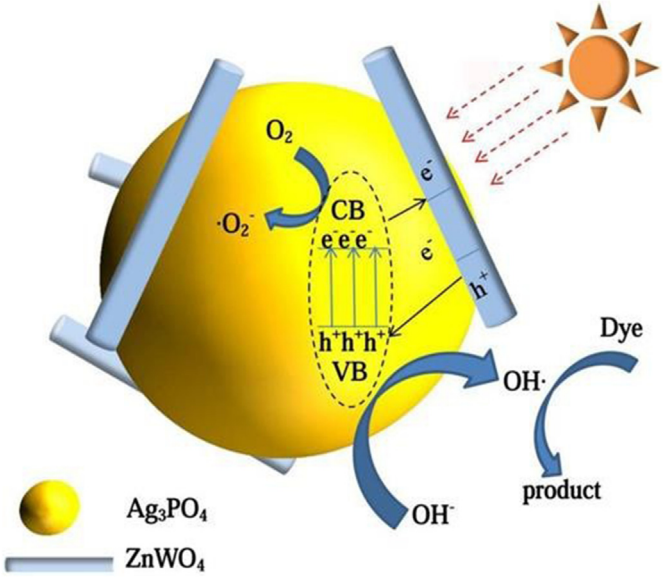

Figure 6. The photocatalytic mechanism under visible light irradiation (Zhang et al., 2017b).

Table 5. Summary of the undoped and co-doped $ZnWO_4$ photocatalyst for the removal of pollutants.

Photocatalyst	Preparation condition	Characterization	Finding	Pollutant	Reference
$ZnWO_4$/ Bentonite	Bentonite (12 wt%), pH = 10, Temp. = 500 °C for 12 h	XRD, SEM, EDS, TEM, XPS, uv-vis, BET, PL	$ZnWO_4$ = Surface area (10.77 m^2/g) $ZnWO_4$/Bentonite = MB removal (98 %), RhB removal (96 %), Bandgap (2.8 eV)	Methylene blue, Rhodamine B	Ida et al. (2019)
$CdS/ZnWO_4$	Stirring time = 8 h, Temp. = 450 °C	XRD, SEM, HRTEM, PL, FTIR, UV-vis, BET, XPS, CV	$ZnWO_4$ = Surface area (11.92 m^2/g), NGB removal (80.1 %), Bandgap (3.15 eV), -1.085–5 A $CdS/ZnWO_4$ = Surface area (18.03 m^2/g), NGB (93.4 %), Band gap (2.19 eV), -2.05–5 A	Naphthol Green B	Jayamani and Shanthi, 2020
$Bi^{3+}/ZnWO_4$	pH = 8.5, Temp. = 180 °C for 24 h	XRD, UV-vis, XPS, SEM, EPR, EDX	$ZnWO_4$ = Bandgap (3.35 eV), NO removal (45.87 %) $Bi^{3+}/ZnWO_4$ = Bandgap (2.77 eV), NO removal (55.29 %)	Nitrogen (II) oxide	Li et al. (2020a,b)
$Ag/ZnWO_4$	Stirring time = 24 h, UV light = 20 mW/cm^2, Temp. = 180 °C	XRD, FTIR, UV-vis, HRTEM, SEM, BET	$ZnWO_4$ = Surface area (53.12 m^2/g), Bandgap (3.87 eV) 0.5-$Ag/ZnWO_4$ = Surface area (22.01 m^2/g) Bandgap = 3.79 eV 3-$Ag/ZnWO_4$ = Surface area (35.23 m^2/g), Bandgap (3.69 eV) MO removal (99.5–90.9 %)	Methyl orange	Li et al. (2020a,b)
$GO/ZnWO_4$	Stirring time = 1 h Temp. = 180 °C for 4 h	XRD, SEM, EDX, UV-vis	$GO/ZnWO_4$ = Bandgap (3.13 eV), TOC removal (62 %), COD removal (54 %)	COD, TOC	Qureshi et al. (2019)
$Fe_3O_4/CeVO_4/ZnWO_4$	Temp. = 550 °C at 3 h	XRD, EDX, FTIR, UV-vis, SEM	$ZnWO_4$ = Bandgap (3.10 eV) $Fe_3O_4/CeVO_4/ZnWO_4$ = Bandgap (2.60 eV), MB removal (84 %)	Methylene blue	Amin-Marsoola et al. (2020)
$Mn/ZnWO_4$	Stirring time = 24 h at 70 °C, Mn dose = 1 wt %, H_2O_2 = 0.5 mM	FTIR, XRD, TEM, EDX, V-vis, BET, XPS, SEM	$ZnWO_4$ = surface area (15.10 m^2/g), Bandgap (4.0 eV), BPA removal (20 %) $Mn/ZnWO_4$ = surface area (11.4 m^2/g), Bandgap (4.1 eV), BPA removal (60 %) $Mn/ZnWO_4/H_2O_2$ = BPA removal (Almost 100 %)	Bisphenol	Anucha et al. (2020)
$Bi_2WO_6/ZnWO_4$	Stirring time = 30 min, pH = 9, Temp. = 180 °C for 24 h, $ZnWO_4$ dose = 5, 10 15 mg	SEM, HRTEM, XRD, EDX, XPS, UV-vis	$ZnWO_4$ = Bandgap (3.52 eV), RhB removal (33 %) BWZW-5 = Bandgap (2.93 e V), RhB removal (77 %) BWZW-10 = Bandgap (2.81 e V), RhB removal (99 %) BWZW-15 = Bandgap (2.87 eV), RhB removal (84 %)	Rhodamine B	Babu et al. (2020)
$ZnO/ZnWO_4$/ AC	ZnO = 1.0 g, Stirring time = 30 min, Temp. = 200 °C for 1 h	FTIR, FESEM, SAED, HRTEM, EDX, XRD, UV-vis	$ZnWO_4$ = Bandgap (3.39 eV), Ampicillin (AMP) removal (44 %) $ZnO/ZnWO_4$ = AMP removal (75 %) $ZnO/ZnWO_4$/AC = Bandgap (3.32 eV), AMP removal (93 %)	Ampicillin	Raizada et al. (2017a)
$ZnWO_4$/EG	EG volume = 0, 50, 62.5, 75 cm^3, Stirring time = 2 h, Temp. = 180 °C for 14 h	HRTEM, XRD, BET, XPS, UV-vis, PL	$ZnWO_4$ = Bandgap (3.89 eV) $ZnWO_4$/EG-50 = Bandgap (3.92 eV) $ZnWO_4$/EG-62.5 = Bandgap (3.94 eV), Cr^{+6} (92.3 %), MB (96.4 %), RhB (93 %), MO (97.7 %) $ZnWO_4$/EG-75 = Bandgap (3.98 eV)	Chromium, Methylene blue, Rhodamine B, Methyl orange	He et al. (2020)
$ZnWO_4$/GO	Stirring time = 30 min, GO = 1, 2, 3, 4 wt%	TEM, XRD, EDX, FTIR, PL, UV, XPS	$ZnWO_4$ = Bandgap (3.35 eV) $ZnWO_4$/GO-3 = Bandgap (3.0 eV), MB removal = 82.85 %	Methylene blue	Mohamed and Bhat, 2017
$ZnWO_4/Mn^{2+}$ $ZnWO_3/Cr^{3+}$ $ZnWO_4/Cu^{2+}$	Stirring time = 90 min, Intensity = 100 W/cm^3 at 40 kHz, temp. = 500 °C at 2 h, $Mn^{2+}/Cr^{3+}/Cu^{2+}$ = 2 mol/ %	XRD, TEM, EDS, XPS, UV-vis, PL	$ZnWO_4$ = Surface area (75.8 m^2/g), Bandgap (3.21 eV) $ZnWO_4/Mn^{2+}$ = Surface area (79.2 m^2/g), Bandgap (2.72 eV) $ZnWO_4/Cr^{3+}$ = Surface area (84.4 m^2/g), Bandgap (2.76 eV) ZnWO4/Cu^{2+} = Surface area (78.8 m^2/g), Bandgap (3.1 eV), MB removal = 100 %	Methylene	Dutta and Raval (2018)
$ZnWO_4$/FACs $ZnWO_4$/FACs/ PoPD	Stirring time = 4 h, pH = 9, FACs = 3 g, Temp. = 180 °C for 24 h Hg lamp = 500 W at 10 min, pH = 4, reaction time = 24 h	XRD, SEM, TEM, UV-vis	$ZnWO_4$ = Bandgap (3.09 eV) $ZnWO_4$/FACs = Bandgap (2.86 eV), TC removal = 53 % $ZnWO_4$/FACs/PoPD = Bandgap (2.69 eV), TC removal = 76.7 %	Tetracycline hydrochloride	Ye et al. (2019)

(*continued on next page*)

Table 5 (*continued*)

Photocatalyst	Preparation condition	Characterization	Finding	Pollutant	Reference
$ZnWO_4$	Stirring time = 2h, Temp. = 180 °C at 0, 5, 10, 14 h	XRD, TEM, EDX, BET, XPS, UV-vis	$ZnWO_4$-0 = Bandgap (3.63 eV) $ZnWO_4$-5 = Bandgap (3.84 eV) $ZnWO_4$-10 = Bandgap (3.90 eV) $ZnWO_4$-14 = Bandgap (3.90 eV) Cr^{+6} removal (96.7 eV)	Chromium	He at al. (2019)
$ZnWO_4$/g-C_3N_4	Mixing ratios ($ZnWO_4$:g-C_3N_4) = 1:1, 1:2, 1:3 Temp. = 300 °C for 4 h	TEM, EDX, FTIR, Pl, UV-vis, XPS, RAMAN, BET	$ZnWO_4$ = Bandgap (3.33 eV) $ZnWO_4$/g-C_3N_4 (1:1) = Surface area (43.67 m^2/g), Bandgap (2.68 eV), RhB removal = 62 % $ZnWO_4$/g-C_3N_4 (1:2) = Surface area (56.8 m^2/g), Bandgap (2.53 eV), RhB removal = 78 % $ZnWO_4$/g-C_3N_4 (1:3) = Surface area (94.8 m^2/g), Bandgap (2.53 eV), RhB removal = 88 %	Rhodamine B	Rathi et al. (2020)
ZnO/$ZnWO_4$	Stirring time = 4 h, Mixing ratio (Zn:ZnW) = 1:1, 3:1, Temp. = 200 °C for 12 h	TEM, XRD, XPS, PL, SEM, UV-vis, BET, FTIR	$ZnWO_4$ = Bandgap (4.0 eV) ZnO/$ZnWO_4$ (1:1) = Surface area (7.9 m^2/g), Bandgap (3.9 eV) ZnO/$ZnWO_4$ (1:3) = Surface area (18.7 m^2/g), Bandgap (3.7 eV) MB (80 %), Amiloride (95 %), Caffeine (<40 %)	Methylene blue, Amiloride, Caffeine	Carvalho et al. (2019)
$ZnWO_4$/Ni–Al-LDH/PVDF	Stirring time = 30 min, Temp. = 160 °C for 12 h	SEM, XRD, FTIR, UV-vis, XPS	$ZnWO_4$ = Bandgap (3.51 eV) $ZnWO_4$/Ni–Al-LDH/PVDF = Bandgap (3.21 eV), MB removal = 93.97 %	Methylene blue	Zhao et al. (2020)
ZnO/$ZnWO_4$	pH = 10, Temp. = 600 °C for 12 h	XRD, BET, SEM, TEM, UV-vis, XPS	$ZnWO_4$ = Bandgap (3.33 eV) ZnO/$ZnWO_4$ = Surface area (5.6 m^2/g), Bandgap (3.25 eV), MO (45 %), Phenol (60.6 %), RhB (96.5 %) removal	Methyl orange, Phenol, Rhodamine B	Jaramillo-Paez et al. (2021)
Co/$ZnWO_4$	Stirring time = 1 h, pH = 8, Co = 0.5, 1, 2 wt%, Temp. = 140 °C for 24 h	XRD, FTIR, TG, XPS, TEM, EDS, UV-vis, PL	$ZnWO_4$ = Bandgap (3.49 eV) Co/$ZnWO_4$ (1 %) = Bandgap (3.23 eV), Cr^{+6} (99 %), RhB (97.80 %) removal	Chromium, Rhodamine B	Alam et al. (2018)
Pd/$ZnWO_4$	Stirring time = 60 min, Pd = 0.4, 0.8, 1.24, 1.65, 2.04 wt%	XRD, TEM, XPS, UV-vis, PL, BET	$ZnWO_4$ = Bandgap (3.34 eV) Pd/$ZnWO_4$ (0.4 %) = Surface area (34 m^2/g), Bandgap (2.97 eV) Pd/$ZnWO_4$ (0.8 %) = Surface area (38 m^2/g), Bandgap (2.84 eV) Pd/$ZnWO_4$ (1.24 %) = Surface area (42 m^2/g), Bandgap (2.69 eV) Pd/$ZnWO_4$ (1.65 %) = Surface area (45 m^2/g), Bandgap (2.73 eV), Atrazine removal (100 %) Pd/$ZnWO_4$ (2.04 %) = Surface area (46 m^2/g), Bandgap (2.72 eV)	Atrazine	Al-Amshany and Hussein (2018)
Cu/Fe/$ZnWO_4$	Stirring time = 1 h, Temp. = 500 °C for 1 h	XRD, SEM, TEM, SAED, FTIR, UV-vis	Bandgap (1.70 eV). ACT (83 %), AMP (100 %), SMX (68 %) removal	Acetaminophen, Ampicillin, Sulphamethoxazole	Alfred et al. (2021)
$NiFe_2O_4$/$ZnWO_4$	Stirring time = 30 min, $ZnWO_4$ = 10, 20, 30 mg, Temp. = 180 °C for 24 h	XRD, SEM, EDS, XPS, HRTEM, UV-vis	$ZnWO_4$ = Band gap (3.492 eV) $NiFe_2O_4$ = Bandgap (1.707 eV) $NiFe_2O_4$/$ZnWO_4$-10 = Bandgap (1.845 eV), TC removal (87 %) $NiFe_2O_4$/$ZnWO_4$-20 = Bandgap (1.784 eV), TC removal (98 %) $NiFe_2O_4$/$ZnWO_4$-30 = Bandgap (1.829 eV), TC removal (75 %)	Tetracycline	Reddy e al. (2020)
Ag_2O/$ZnWO_4$	Stirring time = 4 h, Ag_2O = 0.01, 0.02, 0.03, 0.04 mol/L	XRD, EDS, XPS, BET, SEM	$ZnWO_4$ = Surface area (29.72 m^2/g), Bandgap (3.22 eV) Ag_2O = Bandgap (1.30 eV) Ag_2O/$ZnWO_4$ (0.01) = Surface area (23.40 m^2g), MX removal (70.84 %) Ag_2O/$ZnWO_4$ (0.02) = Surface area (26.61 m2g), MX removal (85.98 %) Ag_2O/$ZnWO_4$ (0.03) = Surface area (27.55 m^2g), MX removal (90.60 %) Ag_2O/$ZnWO_4$ (0.04) = Surface area (23.80 m^2g), MX removal (84.54 %)	Meloxicam	Wang et al. (2021)
Bi/$ZnWO_4$	Stirring time = 20 min, Temp. = 180 °C for 20 h	XRD, XPS, TEM, BET, UV-vis, ESP	$ZnWO_4$ = Surface area (13.78 m^2/g), RhB removal (78.47 %) Bi/$ZnWO_4$ = Surface area (13.92 m^2/g), RhB removal = 91.87 %)	Rhodamine	Wu et al. (2019)

undoped and co-doped $ZnWO_4$ photocatalyst for photodegradation of pollutants in wastewater.

Other researchers like Zhao et al. (2018) took another route and opted to use something other than metal oxides or transition metals. This researcher synthesized a binary noble-metal-free catalyst system containing $ZnLn_2S_4$ and Ln $(OH)_3$ for efficient photocatalysis and water splitting under visible light. The results obtained from characterizations alone were compared with those of $ZnWO_4$ nanoparticles. $ZnLn_2S_4$ microsphere had a spherical structure composed of nanosheets, Ln $(OH)_3$ nanoparticles were rectangular, while $ZnWO_4$ nanoparticles were spherical. The ternary $ZnLn_2S_4$/Ln $(OH)_3$/$ZnWO_4$ nanocomposite had a broad distribution of 3.849 nm, 17.500 nm, and 18.063 nm for $ZnLn_2S_4$, Ln $(OH)_3$ and $ZnWO_4$. It was observed that $ZnWO_4$ and Ln $(OH)_3$ were attached to the surface of the microsphere $ZnLn_2S_4$, and a combination of $Znln_2S_4$ with Ln (OH) formed a new class of earth-abundant cocatalyst suitable for water splitting under sunlight irradiation.

Activated carbon has also been used alongside ZnO to form a nanocomposite with $ZnWO_4$ nanoparticles; the utilization of activated carbon is very promising and exciting, which made it draw the attention of a lot of researchers due to its low cost, porosity as well as large surface area (Abubakar and Labaran, 2021). For instance, Raizada et al. (2017a) focused on the adsorptive and photocatalytic application of ZnO/$ZnWO_4$/AC t to breakdown Ampicillin (AMP) as well as oxytetracycline (OTC) in an aqueous solution, SEM analysis showed uniform displacement and aggregate formation of ZnO/$ZnWO_4$ on the surface of the activated carbon. The photocatalytic degradation efficiency of AMP by ZnO/$ZnWO_4$/AC, AC, ZnO/$ZnWO_4$, $ZnWO_4$ and ZnO was 35 %, 25 %, 12 %, 10 % and 9 % respectively. As for the photolysis of AMP, it can be observed that the highest efficiency was obtained using the ternary system. After that, the pure AC was used, then the binary ZnO/$ZnWO_4$, $ZnWO_4$, and ZnO, while the photocatalysis of OTC was highest when ZnO/$ZnWO_4$/AC was used, followed by ZnO/$ZnWO_4$ nanocomposite.

Many scientists are now focusing on combining metal oxides and tungsten to improve the photocatalytic activity of $ZnWO_4$ nanoparticles. As a result, photoinduced electrons are transferred. Sadiq et al. (2016) studied the photocatalytic performance of RGO-$ZnWO_4$-Fe_3O_4 nanocomposites under visible light irradiation by combining graphene oxides and tungstates to enhance the photocatalytic activity of the nanoparticles. The analyzed XRD data shows crystal planes of $ZnWO_4$ and Fe_3O_4, but none for RGO was detected, and none of the detection peaks for RGO were linked to a small amount of RGO in the sample. SEM micrographs of the samples showed rod-like and spherical morphology for $ZnWO_4$ and Fe_3O_4, respectively. It was also observed that the two were displaced on the surface of RGO. TEM and HRTEM analysis showed that the nanoparticles formed on the RGO sheets ($ZnWO_4$ and Fe_3O_4) were polycrystalline. Photocatalytic experiments were carried out using RGO-$ZnWO_4$ and RGO-$ZnWO_4$-Fe_3O_4, using different amounts of RGO. It was discovered that increasing the amount of RGO up to 3 % wt resulted in a percentage increase in the degradation efficiency to 85 % within 150 min. In contrast, only 60 % degradation efficiency was observed for $ZnWO_4$, while increasing the amount of RGO beyond 3 % decreased the efficiency of the nanocomposite. The ternary 3 %wt RGO-$ZnWO_4$-Fe_3O_4 (0.01 M) nanocomposite has been confirmed to have high efficiency as a photocatalyst under UV irradiation.

Another study utilized solar light to degrade oxytetracycline (OTC); however, in this case, the nanocomposite formed the H_2O_2/$ZnWO_4$/CaO catalytic system. This work was mainly focused on the $ZnWO_4$/CaO binary system, where after characterization and the results were analyzed, it was seen that there was a uniform distribution of $ZnWO_4$ on the surface of CaO led to a reduction in the porosity of the nanocomposite. The authors also reported the formation of rod-like with irregularly arranged spherical particles. Photocatalytic degradation of OTC using the $ZnWO_4$/CaO and H_2O_2/$ZnWO_4$/CaO binary and ternary systems showed that the ternary system was much more effective than the binary system. It was also ascertained that the optimum pH for this particular system is 5 with an initial concentration of OTC at 5.0×10^{-4} M. The authors concluded a synergistic effect under solar irradiation of H_2O_2 in conjugation with $ZnWO_4$/CaO.

Researchers have investigated metal oxide semiconductor coupling to increase the charge separation of photoproduced electron-hole pairs. Hamrouni et al. (2015a,b) study confirmed that mixtures of binary and ternary metal oxide nanocomposites are very effective at photocatalytic degradation of 4-nitrophenol (4-NP) degradation and 4-methoxybenzyl alcohol (4 MBA) oxidation to 4-methoxy benzaldehyde (P-anisaldehyde, PPA). Electrons are transferred from the more cathodic conduction band (ZnO) to the more anodic band (ZnW) ($ZnWO_4$ or SnO_2) under UV light, while holes are transferred from the valence band of $ZnWO_4$ or SnO_2 to that of ZnO. This electron-hole separation increases the lifetime of the charge carriers, thus improving the efficiency of the adsorbed interfacial charge. Furthermore, the separation of photogenerated e-/h + pairs in binary nanocomposites is owing to the local heterojunctions shared by ZnO and SnO_2 or ZnO and $ZnWO_4$, resulting in increased photoactivity. Reduction of 4-NP was also made by the RGO-$ZnWO_4$--Fe_3O_4 ternary nanocomposite because the 4-NP molecule is slightly acidic; it is better absorbed by the catalyst's surface because RGO is good at providing a more negatively charged surface (Sadiq and Bhat, 2016). This study also demonstrated how the presence of $ZnWO_4$ on the catalyst's surface contributed to a better active site for adsorption. It makes interaction with the substrate easier as it works as a reducing agent and a catalyst matrix. Electron transfer over the matrix of RGO being so easy is what makes it an ideal mediator which enables the acceptance of electrons by the molecules of 4-NP and conversion to 4-NP. This combination

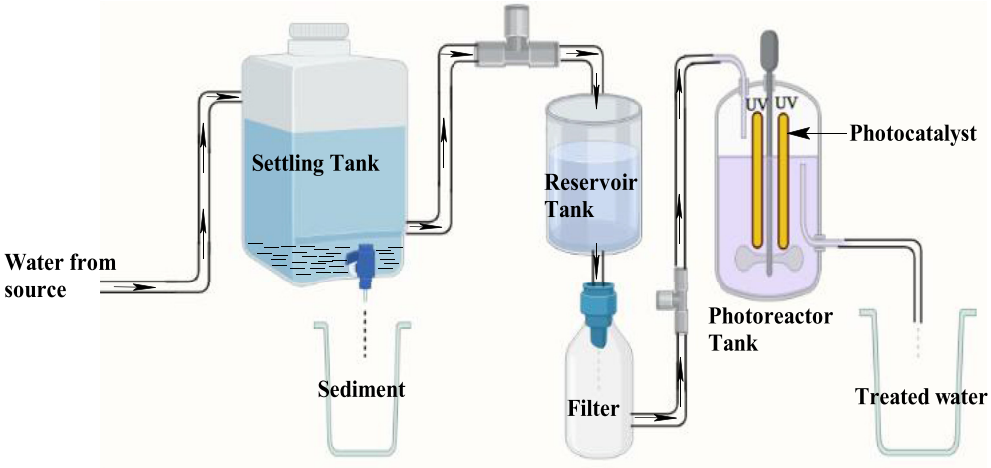

Figure 7. The large scale of wastewater treatment.

gives a favourable synergetic effect to the fast catalytic reduction of 4-NP into 4-AP by $NaBH_4$. The authors also concluded that the nanocomposites are reusable and stable, especially for reduction processes.

Photocatalyst has shown to be a promising nanomaterial as a new frontier of environmental friendly and sustainable wastewater treatment in substituting conventional techniques. Considering the outstanding research efforts for the photodegradation of organic and inorganic pollutants, it is surprising that the industrial applications of water treatment of photocatalytic materials and technologies are still minimal due to low photoconversion efficiency. Implementing advanced oxidation processes such as photocatalysis under sunlight/UV light has been identified as one of the most powerful techniques for removing pollutants from an aqueous solution. Figure 7 is a proposed photocatalysis on a large scale that will play an essential role in tackling environmental issues, mainly organic and inorganic pollutant removal. The advantages of the photocatalysis set-up include safety, environmentally friendly, effortless operation, high decomposition efficacy, and an easy way to utilize photocatalyst via recycling.

7. Conclusion

In summary, the synthesis of $ZnWO_4$ nanoparticles using different methods has been provided. The strategy to improve the catalytic activity of $ZnWO_4$ in the visible region through doping and co-doping with metals, non-metals, and metal oxides has been reviewed. The use of $ZnWO_4$ nanoparticles as photocatalysts to degrade various organic compounds, particularly dyes, and their antimicrobial potential are also discussed. Based on these findings, the following conclusions were reached.

XRD analysis showed that doping had no major effect on the spectra of $ZnWO_4$ the nanoparticle, instead of making the materials more crystalline even though no extra bands formed that could be associated with the dopants used. In most cases, the bands became sharper, and doping improved the efficiency of the nanoparticles. In most cases, the dopants have a lower ionic radius than either Zn^{2+} and W^{6+}, so the dopant ends up latching itself to the surface of the photocatalyst. As more research is coming up on doped $ZnWO_4$ nanoparticles, it has also been reported that the concentration of the dopants may play a huge role in determining the efficiency of the final product. This is so because every combination of nanoparticles with a dopant has an optimum concentration of dopant, which, when reached, the nanoparticle is the most efficient. In most cases, once the concentration has been exceeded, the efficiency of the doped nanoparticles drops. The literature has proven that $ZnWO_4$ is only active under UV light; however, upon doping, the material becomes active under visible light irradiation. Further analysis has shown an order of efficiency to be multiple doped > co-doped > mono-doped > pure $ZnWO_4$. This is a promising material with applications in numerous fields. In the future, $ZnWO_4$ can be doped to form a composite made up of $ZnWO_4$, metals having different properties and nonmetals with different properties at the optimum ratio for various applications, thereby harnessing the numerous benefits that come with using each element in the field of catalysis.

Declarations

Author contribution statement

All authors listed have significantly contributed to the development and the writing of this article.

Funding statement

This research did not receive any specific grant from funding agencies in the public, commercial, or not-for-profit sectors.

Data availability statement

No data was used for the research described in the article.

Declaration of interests statement

The authors declare no conflict of interest.

Additional information

No additional information is available for this paper.

References

Abdolrahmany, A., Mamoory, R.S., Mohammadi, K., 2015. Synthesis of $ZnWO_4$ nano particles by co-precipitation method using central composite design (CCD). In: 10th Biennial congress of the Iranian Ceramic Society, Materials and Energy Research center. Karaj, Iran.

Abubakar, H.L., Labaran, N.T., 2021. Evaluation of the efficiency of constructed activated carbon for the treatment of abattoir wastewater. Sci. World J. 16 (No 2), 172–178.

Aghalari, Z., Dahms, H.U., Sillanpaa, M., 2021. Investigating the effectiveness of nanotechnologies in environmental health journals. Life Sci Soc Pol 17 (8).

Ahmad, T., Farooq, U., Phul, R., 2018. Fabrication and photocatalytic applications of perovskite materials with special emphasis on alkali-metal-based niobates and tantalates. Ind. Eng. Chem. Res. 57 (1), 18–41.

Ahmed, A.I., Kospa, D.A., Gamal, S., Samra, S.E., Salah, A.A., El-Hakam, S.A., Ibrahim, A.A., 2022. Fast and simple fabrication of reduced graphene oxide-zinc tungstate nanocomposite with enhanced photoresponse properties as a highly efficient indirect sunlight driven photocatalyst and antibacterial agent. J. Photochem. Photobiol. Chem. 113907.

Al-Amshany, Z.M., Hussein, M.A., 2018. Novel Pd/$ZnWO_4$ nanocomposite materials for photocatalytic degradation of atrazine. Appl. Nanosci. 8 (3), 527–536.

Alam, U., Khan, A., Bahnemann, D., Muneer, M., 2018. Synthesis of Co-doped $ZnWO_4$ for simultaneous oxidation of RhB and reduction of Cr(VI) under UV-light irradiation. J. Environ. Chem. Eng. 6 (4), 4885–4898.

Alfred, M.O., Moodley, R., Oladoja, N.A., Omorogie, M.O., Adeyemi, O.G., Olorunnisola, D., Msagati, T.A.M., de Jesus Motheo, A., Unuabonah, E.I., 2021. Sunlight-active Cu/Fe@ $ZnWO_4$-kaolinite composites for degradation of acetaminophen, ampicillin and sulfamethoxazole in water. Ceram. Int. 47 (13), 19220–19233.

Alshehri, S.M., Ahmed, J., Ahamad, T., Alhokbany, N., Arunachalam, P., Al-Mayouf, A.M., Ahmad, T., 2018. Synthesis, characterization, multifunctional electrochemical (OGR/ORR/SCs) and photodegradable activities of $ZnWO_4$ nanobricks. J. Sol. Gel Sci. Technol. 87 (1), 137–146.

Amin-Marsooli, M., Rahimi Nasrabadi, M., Fasihi-Ramandi, M., Adib, K., Pourmasoud, S., Ahmadi, F., Eghbali, M., Sobhani Nasab, A., Tomczykowa, M., Plonska-Brzezinska, M.E., 2020. Synthesis of magnetic Fe_3O_4/$ZnWO_4$ and Fe_3O_4/$ZnWO_4$/$CeVO_4$ nanoparticles: the photocatalytic effects on organic pollutants upon irradiation with UV-Vis light. Catalysts 10 (5), 494.

Amouzegar, Z., Naghizadeh, R., Rezaie, H.R., Ghahari, M., Aminzare, M., 2015. Microwave engineering of $ZnWO_4$ nanostructures: towards morphologically favorable structures for photocatalytic activity. Ceram. Int. 41 (7), 8352–8359.

Anucha, C.B., Altin, I., Biyiklioglu, Z., Bacaksiz, E., Polat, I., Stathopoulos, V.N., 2020. Synthesis, characterization, and photocatalytic evaluation of manganese (III) phthalocyanine sensitized $ZnWO_4$ ($ZnWO_4$MnPc) for bisphenol a degradation under UV irradiation. Nanomaterials 10 (11), 2139.

Arularasu, M.V., Sundaram, R., 2016. Synthesis and characterization of nanocrystalline $ZnWO_4$ -ZnO composites and their humidity sensing performance. Sens. Bio Sens. Res. 11, 20–25.

Atla, R., Oh, T.H., 2021. Solar light-driven 2D MoS2 nanoflake-supported 1D $ZnWO_4$ nanorod heterostructure: efficient separation of charge carriers for removing toxic organic pollutants. J. Environ. Chem. Eng. 9 (6), 106427.

Babooram, K., 2008. Novel solution routes to ferroelectrics and relaxors. Handbook of Advanced Dielectric. Piezoelec. Ferroelec. Mater. 852–883.

Babu, B., Koutavarapu, R., Shim, J., Yoo, K., 2020. Enhanced solar light–driven photocatalytic degradation of tetracycline and organic pollutants by novel one–dimensional $ZnWO_4$ nanorod–decorated two–dimensional Bi_2WO_6 nanoflakes. J. Taiwan Inst. Chem. Eng. 110, 58–70.

Bai, X., Wang, L., Zhu, Y., 2012. Visible photocatalytic activity enhancement of $ZnWO_4$ by graphene hybridization. ACS Catal. 2 (12), 2769–2778.

Bavykina, I., Angloher, G., Hauff, D., Kiefer, M., Petricca, F., Probst, F., 2009. Development of cryogenic phonon detectors based on CaMoO4 and $ZnWO_4$ scintillating crystals for direct dark matter search experiments. Opt. Mater. 31 (10), 1382–1387.

Bøjesen, E.D., Jensen, K.M.Ø., Tyrsted, C., Mamakhel, A., Andersen, H.L., Reardon, H., Chevalier, J., Dippel, Iversen, B.B., 2016. The chemistry of $ZnWO_4$ nanoparticle formation. Chem. Sci. 7 (10), 6394–6406.

Burstein, E., 1954. Anomalous optical absorption limit in InSb. Phys. Rev. 93 (3), 632–633.

Carvalho, K.T.G., Lopes, O.F., Ferreira, D.C., Ribeiro, C., 2019. ZnO:$ZnWO_4$ heterostructure with enhanced photocatalytic activity for pollutant degradation in liquid and gas phases. J. Alloys Compd. 797, 1299–1309.

Cauerhff, A., Castro, G.R., 2013. Bionanoparticles, a green nanochemistry approach. Electron. J. Biotechnol. 16 (3).

Chen, S.H., Wang, B.X., Qiu, X.H., Xiong, Z.S., 2013. Photoreactive carbon and nitrogen-codoped $ZnWO_4$ nanoparticles: synthesis and reactivity. Adv. Mater. Res. 621, 172–177.

Chena, G., Wanga, F., Yu, J., Zhang, H., Zhang, X., 2017. Improved red emission by codoping Li^{3+} in $ZnWO_4$:Eu^{3+} phosphors. J. Mol. Struct. 1128, 1–4.
Cholan, S., Shanmugam, N., Kannadasan, N., Sathishkumar, K., Deivam, K., 2014. Effect of poly ethylene glycol (PEG) as surfactant on cerium doped ZnS nanoparticles. J. Mater. Res. Technol. 3 (3), 222–227.
Dehsari, S.H., Ribeiro, H.A., Ersoz, B., Tremel, W., Jakob, G., Asadi, K., 2017. Effect of precursor concentration on size evolution of iron oxide nanoparticles. CrystEngComm 19 (44), 6694–6702.
Dutta, D.P., Raval, P., 2018. Effect of transition metal ion (Cr^{3+}, Mn^{2+} and Cu^{2+}) doping on the photocatalytic properties of $ZnWO_4$ nanoparticles. J. Photochem. Photobiol. Chem. 357, 193–200.
Ede, S.R., Ramadoss, A., Nithiyanantham, U., Anantharaj, S., Kundu, S., 2015. Bio-molecule Assisted Aggregation of $ZnWO_4$ Nanoparticles (NPs) into Chain-like.
Emsaki, M., Hassanzadeh, S.A., Teluri, S.A., 2018. Microemulsion synthesis of ZnO $ZnWO_4$ nanoparticles for superior photodegradation of organic dyes in water. J. Mater. Sci. Mater. Electron. 29, 2384–2391.
Enesca, A., 2021. The influence of photocatalytic reactors design and operating parameters on the wastewater organic pollutants removal – a mini review. Catalysts 11 (5).
Faka, V., Tsoumachidou, S., Moschogiannaki, M., Kiriakidis, G., Poulios, I., Binas, V., 2021. $ZnWO_4$ nanoparticles as efficient photocatalyst for degradation of para-aminobenzoic acid: impact of annealing temperature on photocatalytic performance. J. Photochem. Photobiol. Chem., 113002
Faraday, M., 1987. Experimental relations of gold (and other metals) to light. Phil. Transact. Royal Soc. B 147, 145–181.
Garadkar, K.M., Ghule, L.A., Sapnar, K.B., Dhole, S.D., 2013. A facile synthesis of $ZnWO_4$ nanoparticles by microwave assisted technique and its application in photocatalysis. Mater. Res. Bull. 48, 1105–1109.
Gautam, S., Agrawal, H., Thakur, M., Akbari, A., Sharda, H., Kaur, R., Amini, M., 2020. Metal oxides and metal organic frameworks for the photocatalytic degradation: a review. J. Environ. Chem. Eng. 103726.
Geetha, G.V., Sivakumar, R., Ganesh, V., Sanjeeviraja, C., 2019. Properties of polymeric surfactant mediated $ZnWO_4$ nanoparticles for photocatalytic application. In: Proceedings of the International Conference on Advanced Materials: ICAM 2019.
Geetha, G.V., Keerthana, S.P., Madhuri, K., Sivakumar, R., 2021a. Effect of solvent volume on the properties of $ZnWO_4$ nanoparticles and their photocatalytic activity for the degradation of cationic dye. Inorg. Chem. Commun. 132, 108810.
Geetha, G.V., Sivakumar, R., Sanjeeviraja, C., Ganesh, V., 2021b. Photocatalytic degradation of methylene blue dye using $ZnWO_4$ catalyst prepared by a simple co-precipitation technique. J. Sol. Gel Sci. Technol. 97 (3), 572–580.
Gouveia, A.F., Assis, M., Cavalcante, L.S., Gracia, L., Longo, E., Andres, J., 2018. Reading at exposed surfaces: theoretical insights into photocatalytic activity of $ZnWO_4$. Front. Res. Today 1, 1005.
Grabis, J., Jankovica, D., Kodols, M., Rasmane, D., 2012. Photocatalytic activity of $ZnWO_4$ nanoparticles prepared by combustion synthesis. Latv. J. Chem. 51 (1-2), 93–98.
Greco, F., Zucca, A., Taccola, S., Menciassi, A., Fujie, T., Haniuda, H., Takeoka, S., Dario, P., Mattoli, V., 2011. Ultra-thin conductive free-standing PEDOT/PSS nanofilms. Soft Matter 7, 10642–10650.
Grossin, D., 2021. Encyclopedia of materials: technical ceramics and glasses. Phosphates 3, 567–574.
Hamrouni, A., Moussa, N., Di Paola, A., Palmisano, L., Houas, A., Parrino, F., 2015a. Photocatalytic activity of binary and ternary SnO_2–ZnO–$ZnWO_4$ nanocomposites. J. Photochem. Photobiol. Chem. 309, 47–54.
Hamrouni, A., Moussa, N., Di Paola, A., Parrino, F., Houas, A., Palmisano, L., 2015b. Characterization and photoactivity of coupled ZnO–$ZnWO_4$ catalysts prepared by a sol–gel method. Appl. Catal. B Environ. 154–155, 379–385.
Hao, Y., Zhang, L., Zhang, Y., Zhao, L., Zhang, B., 2017. Synthesis of pearl necklace-like ZnO–$ZnWO_4$ heterojunctions with enhanced photocatalytic degradation of Rhodamine B. RSC Adv. 7 (42), 26179–26184.
Haque, S., Nawrot, D.A., Alakurtti, S., Ghemtio, L., Yli-Kauhaluoma, J., Tammela, P., 2014. Screening and characterization of antimicrobial properties of semisynthetic botulin derivatives. PLoS One 9 (7), e102696.
He, G., Fan, H., Ma, L., Wang, K., Ding, D., Liu, C., Wang, Z., 2016. Synthesis, characterization and optical properties of nanostructured $ZnWO_4$. Mater. Sci. Semicond. Process. 41, 404–410.
He, H., Luo, Z., Tang, Z.Y., Yu, C., 2019. Controllable construction of $ZnWO_4$ nanostructure with enhanced performance for photosensitized Cr(VI) reduction. Appl. Surf. Sci. 490, 460–468.
He, H., Luo, Z., Yu, C., 2020. Multifunctional $ZnWO_4$ nanoparticles for photocatalytic removal of pollutants and disinfection of bacteria. J. Photochem. Photobiol. Chem. 401, 112735.
Hosseinpour-Mashkani, S.M., Maddahfar, M., Sobhani-Nasab, A., 2016. Precipitation synthesis, characterization, morphological control, and photocatalyst application of $ZnWO_4$ nanoparticles. J. Electron. Mater. 45 (7), 3612–3620.
Hu, C., Song, L., Zhang, Z., Chen, N., Feng, Z., Qu, L., 2015. Tailored graphene systems for unconventional applications in energy conversion and storage devices. Energy Environ. Sci. 8 (1), 31–54.
Ida, G., Thirumalai, K., Swaminathan, M., Easwaramoorthy, D., 2019. Photocatalytic activity of natural clay Bentonite supported $ZnWO_4$. Indian J. Chem. 58, 637–644.
Iskandar, F., Fitriani, P., Merissa, S., Mukti, R.R., Khairurrijal, Abdullah, M., 2014. Fe_3O_4/Zeolite nanocomposites synthesized by microwave assisted coprecipitation and its performance in reducing viscosity of heavy oil. AIP Conf. Proc. 1586, 132–135.
Jaramillo-Paez, C., Navıo, J.A., Puga, F., Hidalgo, M.C., 2021. Sol-Gel synthesis of $ZnWO_4$-(ZnO) composite materials. Characterization and photocatalytic properties. J. Photochem. Photobiol. A: Chemistry 404, 112962.
Jayamani, G., Shanthi, M., 2020. An efficient nanocomposite CdS-$ZnWO_4$ for the degradation of Naphthol Green B dye under UV-A light illumination. Nano Struct. Nano Objects 22, 100452.
Jeong, H.Y., Lim, H.S., Lee, J.H., Heo, J., Kim, H.N., Cho, S.O., 2020. $ZnWO_4$ nanoparticle scintillators for high resolution X-ray imaging. Nanomaterials 10 (9), 1721.
Kim, D.W., Cho, I.S., Shin, S.S., Lee, S., Noh, T.H., Kim, D.H., Jung, H.S., Hong, K.S., 2011. Electronic band structures and photovoltaic properties of MWO_4 (M= Zn, Mg, Ca, Sr) compounds. J. Solid State Chem. 184 (8), 2103–2107.
Koutavarapu, R., Reddy, C.V., Syed, K., Reddy, K.R., Saleh, T.A., Lee, D.Y., Shim, J., Aminabhavi, T.M., 2022. Novel Z-scheme binary zinc tungsten oxide/nickel ferrite nanohybrids for photocatalytic reduction of chromium (Cr (VI)), photoelectrochemical water splitting and degradation of toxic organic pollutants. J. Hazard Mater. 423, 127044.
Kumari, V., Mittal, A., Jindal, Yadav S., Kumar, N., 2019. S-, N- and C- doped ZnO as semiconductor photocatalysts: a review. Front. Mater. Sci. 13 (1), 1–22.
Li, C., Du, X., Yue, D., Gao, J., Wang, Z., 2013. Full-color emission based $ZnWO_4$ spherical nanoparticles through doping of rare earth ions. Mater. Lett. 108, 257–260.
Li, M., Zhu, Q., Li, J.G., Kim, B.N., 2020a. Elongation of ZnWO4 nanocrystals for enhanced photocatalysis and the effects of Ag decoration. Appl. Surf. Sci. 515, 146011.
Li, S., Chang, L., Peng, J., Gao, J., Lu, J., Zhang, F., Zhu, G., Hojamberdiev, M., 2020b. Bi0 nanoparticle loaded on Bi^{3+}-doped $ZnWO_4$ nanorods with oxygen vacancies for enhanced photocatalytic NO removal. J. Alloys Compd. 818, 52837.
Liu, Z., Tian, J., Zeng, D., Yu, C., Zhu, L., Huang, W., Yang, K., Li, D., 2017. A facile microwave-hydrothermal method to fabricate B doped $ZnWO_4$ nanorods with high crystalline and highly efficient photocatalytic activity. Mater. Res. Bull. 94, 298–306.
Lounis, S.D., Runnerstrom, E.L., Bergerud, A., Nordlund, D., Milliron, D.J., 2014. Influence of dopant distribution on the plasmonic properties of Indium tin oxide nanocrystals. J. Am. Chem. Soc. 136, 7110–7116.
Luo, Z., Xu, D., Zhang, S., Shen, J., 2018. Facile hydrothermal synthesis of $ZnWO_4$ for enhanced photocatalytic performance. J. Nanosci. Nanotechnol. 18 (10), 7241–7245.
Majhi, K.C., Yadav, M., 2021. Synthesis of inorganic nanomaterials using carbohydrates. Green Inorgan. Syn. 5, 109–135.
Marsooli, A.M., Nasrabadi, R.M., Fasihi-Ramandi, M., Adib, K., Pourmasoud, S., Ahmadi, F., Eghbali, M., Nasab, A.S., Tomczykowa, M., Plonska-Brzezinska, M.E., 2020. Synthesis of magnetic Fe_3O_4/$ZnWO_4$ and Fe_3O_4/$ZnWO_4$/$CeVO_4$ nanoparticles: the photocatalytic effects on organic pollutants upon irradiation with UV-vis light. Catalysts 10 (5), 494.
Mehdi, R., Mahdi, P.S., Rezvani, Adib Z., Ganjali, K., Reza, M., 2015. Facile synthesis optimization and structure characterization of zinc tungstate nanoparticles. Mater. Manuf. Process. 30 (1), 34–40.
Mendes-Felipe, C., Veloso-Fernandez, A., Vilas-Vilela, J.L., Ruiz-Rubio, L., 2022. Hybrid organic–inorganic membranes for photocatalytic water remediation. Catalysts 12 (2), 180.
Mohamed, M.J.S., Bhat, D.K., 2017. Novel $ZnWO_4$/RGO nanocomposite as high performance photocatalyst. AIMS Mater. Sci. 4 (1), 158–171.
Mosleh, M., Taherinejat, K., 2016. Simple synthesis and characterization of zinc tungstate nanoparticles with the aid of surfactants and investigation of its photocatalyst application. J. Mater. Sci. Mater. Electron. 27 (10).
Moss, T.S., 1954. The interpretation of the properties of Indium Antimonide. Proc. Phys. Soc. B 67, 775–782.
Neto, N.A., Nunes, T.B.O., Li, M., Longo, E., Bomio, M.R.D., Motta, F.V.D., 2020. Influence of microwave-assisted hydrothermal treatment time on the crystallinity, morphology and optical properties of $ZnWO_4$ nanoparticles: photocatalytic activity. Ceram. Int. 46 (2), 1766–1774.
Paliki, A.K., Suresh, P., Sailja, V.B., 2016. Rapid visible light photocatalytic degradation of organic pollutants using $ZnWO_4$ nanoparticles. Int. J. Eng. Appl. Sci. Technol. 1 (8), 183.
Paliki, A.K., Botsa, S.M., Sailaja, B.B.V., 2018. Catalytic activity of graphene oxide hybridized $ZnWO_4$ for dyes degradation and oxidation of functionalized benzyl alcohols. MOJ Biorgan. Organ. Chem. 2 (5), 230–234.
Patra, K., Baek, K.H., 2014. Green nanobiotechnology: factors affecting synthesis and characterization techniques. J. Nanomater. 2014, 1–12.
Pavithra, N.S., Nagaraju, G., Patil, S.B., 2021. Ionic liquid-assisted hydrothermal synthesis of $ZnWO_4$ nanoparticles used for photocatalytic applications. Ionics 27, 3533–3541.
Phung, H.N.T., Tran, V.N.K., Duong, P.H., Le, H.V.T., Truong, N.D., 2017. Effect of co-doping and tri-doping with transition metals and a non-metal on photocatalytic activity in the visible light of TiO_2 thin film. J. Kor. Phys. Soc. 70, 995–1000.
Qureshi, K., Ahmad, M.Z., Bhatti, I.A., Zahid, M., Nisar, J., Iqbal, M., 2019. Graphene oxide decorated $ZnWO_4$ architecture synthesis, characterization and photocatalytic activity evaluation. J. Mol. Liq. 285, 778–789.
Rahmani, M., Sedaghat, T., 2019. B. Nitrogen-doped $ZnWO_4$ nanophotocatalyst: synthesis, characterization and photodegradation of methylene blue under visible light. Res. Chem. Intermed. 45, 5111–5124.
Rahnamaeiyan, S., Nasiri, M., Alborzi, A., Tabatabaei, S.M., 2015. Sonochemical synthesis and characterization of zinc tungstate nanoparticles and investigation of its photocatalyst application. J. Mater. Sci. Mater. Electron. 27 (2), 1113–1117.
Raizada, P., Kumari, J., Shandilya, P., Singh, P., 2017a. Kinetics of photocatalytic mineralization of oxytetracycline and ampicillin using activated carbon supported ZnO/$ZnWO_4$ nanocomposite in simulated wastewater. Desalination Water Treat. 79, 204–213.
Raizada, P., Shandilya, P., Singh, P., Thakur, P., 2017b. Solar light-facilitated oxytetracycline removal from the aqueous phase utilizing a H_2O_2/$ZnWO_4$/CaO catalytic system. J. Taibah Univ. Sci. 11 (5), 689–699.
Rajakumaran, R., Krishnapandi, A., Chen, S.-M., Balamurugan, K., Chang, F.M., Sakthinathan, S., 2021. Electrochemical investigation of zinc tungstate nanoparticles;

a robust sensor platform for the selective detection of furazolidone in biological samples. Microchem. J. 160, 105750.
Rao, B.G., Mukherjee, D., Reddy, B.M., 2017. Novel approaches for preparation of nanoparticles: synthesis, characterization and applications. Nanostruc. Novel Ther. 1–36.
Rao, C., Zhang, W., Hu, Z., Feng, Z., Chen, Y., Pan, Y., Hu, P., Wang, Y., Zhao, W., 2019. Enhancing the photocatalytic activity of La/Y Co-doped $ZnWO_4$ under UV irradiation. Key Eng. Mater. 842, 214–222.
Rathi, V., Panneerselvam, A., Sathiyapriya, R., 2020. Graphitic carbon nitride (g-C_3N_4) decorated $ZnWO_4$ heterojunctions architecture synthesis, characterization and photocatalytic activity evaluation. Diam. Relat. Mater. 108, 107981.
Reddy, C.V., Koutavarapu, R., Reddy, K.R., Shetti, N.P., Aminabhavi, T.M., Shim, J., 2020. Z-scheme binary 1D $ZnWO_4$ nanorods decorated 2D $NiFe_2O_4$ nanoplates as photocatalysts for high efficiency photocatalytic degradation of toxic organic pollutants from wastewater. J. Environ. Manag. 268 (15), 110677.
Sadiq, M.J., Bhat, D.K., 2016. Novel RGO-ZnWO4-Fe_3O_4 nanocomposite as an efficient catalyst for rapid reduction of 4-nitrophenol to 4-aminophenol. Ind. Eng. Chem. Res. 55 (27), 7267–7272.
Sadiq, M.J., Bhat, D.K., 2017a. Novel $ZnWO_4$/RGO nanocomposite as high performance photocatalyst. AIMS Mater. Sci. 4 (1), 158–171.
Sadiq, M.M.J., Shenoy, U.S., Bhat, D.K., 2016. Novel RGO–$ZnWO_4$–Fe_3O_4 nanocomposite as high-performance visible light photocatalyst. RSC Adv. 6 (66), 61821–61829.
Saito, N., Matsumoto, H., Kobayashi, H., Ikarashi, K., Nishiyama, H., Inoue, Y., 2004. A new photocatalyst of RuO_2-loaded $PbWO_4$ for overall splitting of water. Chem. Lett. 133, 1452–1453.
Schimpf, A.M., Lounis, S.D., Runnerstrom, E.L., Milliron, D.J., Gamelin, D.R., 2014. Redox chemistries and plasmon energies photoshopped ln_2O_3 and Sn-doped ln_2O_3 (ITO) nanocrystals. J. Am. Chem. Soc.
Seong, S., Yee, K.A., Albright, T.A., 1993. Interlayer communication in some two-dimensional materials. J. Am. Chem. Soc. 115, 1981–1987.
Sethi, Y.A., Panmand, R.P., Ambalkar, A.A., Kulkarni, A.K., Gunjal, A., Gosavi, S.W., Kulkarni, V.M., Patil, D.R., Kale, B.B., 2019. In situ preparation of CdS decorated $ZnWO_4$ nanorods as a photocatalyst for direct conversion of sunlight into fuel and RhB degradation. Sustain. Energy Fuels 3, 793–800.
Severo, E.C., Abaide, E.R., Anchieta, C.G., Foletto, V.S., Weber, C.T., Garlet, T.B., Collazzoa, G.C., Mazutti, M.A., Gündel, A., Kuhna, R.C., Foletto, E.L., 2016. Preparation of zinc tungstate ($ZnWO_4$) particles by solvo-hydrothermal technique and their application as support for inulinase immobilization. Mater. Res. 19 (4), 781–785.
Sharma, R.K., Mudring, A., Ghosh, P., 2017. Recent trends in binary and ternary rare-earth fluoride nanophosphors: how structural and physical properties influence optical behaviour. J. Lumin. 189, 44–63.
Singh, M., Manikandan, S., Kumaraguru, A.K., 2011. Nanoparticles: a new technology with wide applications. Res. J. Nanosci. Nanotechnol. 1 (1), 1–11.
Singh, N.P., Devi, Y.R., Singh, N.R., Singh, N.M., 2019. Synthesis of Tb^{3+} ion doped $ZnWO_4$ phosphors and investigation of their photoluminescence properties: concentration effect. Bull. Mater. Sci. 42 (3).
Sivaganesh, D., Saravanakumar, S., Sivakumar, V., Rajajeyaganthan, R., Arunpandian, M., Gopal, J.N., Thirumalaisamy, T.K., 2020. Surfactants-assisted synthesis of $ZnWO_4$ nanostructures: a view on photocatalysis, photoluminescence and electron density distribution analysis. Mater. Char. 159, 110035.
Somorjai, G.A., Park, J.Y., 2008. Colloid science of metal nanoparticle catalysts in 2D and 3D structures. Challenges of nucleation, growth, composition, particle shape, size control and their influence on activity and selectivity. Top. Catal. 49 (3-4), 126–135.
Su, Y., Zhu, B., Guan, K., Gao, S., Lv, L., Du, C., Peng, L., Hou, L., Wang, X., 2012. Particle Size and Structural Control of $ZnWO_4$ Nanocrystals via Sn^{2+} Doping for Tunable.
Tang, Z., Li, X., Yang, J., Yu, J., Wang, J., Tang, Z., 2014. Mixed potential hydrogen sensor using $ZnWO_4$ sensing electrode. Sensor. Actuator. B Chem. 195, 520–525.
Tian, L., Rui, Y., Sun, K., Cui, W., An, W., 2018. Surface decoration of $ZnWO_4$ nanorods with Cu_2O nanoparticles to build heterostructure with enhanced photocatalysis. Nanomaterials 8 (1), 33.
Wang, Y., Liping, L., Li, G., 2017. Solvothermal synthesis, characterization and photocatalytic performance of Zn-rich $ZnWO_4$ nanocrystals. Appl. Surf. Sci. 393, 159–167.
Wang, X., Yu, S., Li, Z.H., He, L.L., Liu, Q.L., Hu, M.Y., Xu, L., Wang, X.F., Xiang, Z., 2021. Fabrication Z-scheme heterojunction of Ag_2O/$ZnWO_4$ with enhanced sonocatalytic performances for meloxicam decomposition: increasing adsorption and generation of reactive species. Chem. Eng. J. 405, 126922.
WHO, 2021. Antimicrobial Resistance. www.who.int/health-topics/antimicrobial-resistance.
Wu, Y., Zhou, S., He, T., Jin, X., Lun, L., 2019. Photocatalytic activities of $ZnWO_4$ and Bi@ $ZnWO_4$ nanorods. Appl. Surf. Sci. 484, 409–413.
Xiong, G., Zhang, W., Hu, Z., Feng, Z., Hu, P., Ma, L., Pan, Y., Wang, Y., Luo, L., 2018. Photocatalytic activity of $ZnWO_4$ phosphors doped with Li impurities. J. Lumin. 206, 370–375.
Xu, C., Qu, X., 2014. Cerium oxide nanoparticle: a remarkably versatile rare earth nanomaterial for biological applications. NPG Asia Mater. 6, e90.
Yadav, R.S., Dhoble, S.J., Rai, S.B., 2018. Enhanced photoluminescence in Tm^{3+}, Yb^{3+}, Mg^{2+} tri-doped $ZnWO_4$ phosphor: three photon upconversion, laser induced optical heating and temperature sensing. Sens. Actuators, B 273, 1425–1434.
Yan, J., Shen, Y., Li, F., Li, T., 2013. Synthesis and photocatalytic properties of $ZnWO_4$ nanocrystals via a fast microwave-assisted method. Sci. World J., 458106
Yan, X., Zhnag, C., Zhong, G., Li, J., 2019. Tuning the electronic and magnetic properties of metal-doped phenanthrene by codoping method. AIP Adv. 9, 035104.
Yang, Y., Scholz, R., Fan, J.H., Dietrich, H., Gosele, U., Zacharias, M., 2009. Multitwinned spinel nanowires by assembly of nanobricks via oriented attachment: a case study of Zn_2TiO_4. ACS Nano 3 (3), 555–562, 2009.
Yang, K., Zhang, Y.F., Li, Y., Huang, P., Chen, X., Dai, W.X., Fu, X.Z., 2016a. Insight into the function of alkaline earth metal oxides as electron promoters for Au/TiO_2 catalysts used in CO oxidation. Appl. Catal. B Environ. 183, 206–215.
Yang, Y., Zhu, J., Shi, W., Zhou, J., Gong, D., Gu, S., Wang, S., Xu, Z., Lu, B., 2016b. 3D nanoporous ZnWO4 nanoparticles with excellent electrochemical performances for supercapacitors. Mater. Lett. 177, 34–38.
Yao, C., Lin, Y., Yuan, J., Liao, L., Zhu, M., Weng, L., Yang, J., Wu, Z., 2015. Mono-cadmium vs mono-mercury doping of Au25 nanoclusters. J. Am. Chem. Soc. 137 (49), 15350–15353.
Ye, L., Zhang, T., Shao, S., Yang, L., Cai, Y., Guan, W., 2019. Synthesis of poly-o-phenylenediamine (PoPD)/$ZnWO_4$ supported on the fly-ash cenospheres with enhanced photocatalytic performance under visible light. Mater. Lett. 236, 370–373.
Yesuraj, J., Suthanthiraraj, S.A., 2019. Bio-molecule templated hydrothermal synthesis of $ZnWO_4$ nanomaterial for high-performance supercapacitor electrode application. J. Mol. Struct. 1181, 131–141.
Yu, H.J., Shi, R., Zhao, Y.F., Waterhouse, G.I.N., Wu, L.Z., Tung, C.H., Zhang, T.R., 2016. Smart utilization of carbon dots in semiconductor photocatalysis. Adv. Mater. 28, 9454–9477.
Zhai, B., Yang, L., Huang, Y., 2019. Intrinsic defect engineering in Eu^{3+} doped $ZnWO_4$ for annealing temperature tunable photoluminescence. Nanomaterials 9 (1), 99.
Zhang, L., Wang, Z., Wang, L., Xing, Y., Li, X., Zhang, Y., 2014a. Electrochemical performance of $ZnWO_4$/CNTs composite as anode materials for lithium-ion battery. Appl. Surf. Sci. 305, 179–185.
Zhang, C., Zhang, H., Zhang, K., Li, X., Leng, Q., Hu, C., 2014b. Photocatalytic activity of $ZnWO_4$: band structure, morphology and surface modification. ACS Appl. Mater. Interfaces 6 (16), 14423–14432.
Zhang, J., Tse, K., Wong, M., Zhang, Y., Zhu, T., 2016. A brief review of co-doping. Front. Phys. 11, 117405.
Zhang, N., Chen, D., Cai, B., Wang, S., Niu, F., Qin, L., Huang, Y., 2017a. Facile synthesis of CdS$ZnWO_4$ composite photocatalysts for efficient visible light driven hydrogen evolution. Int. J. Hydrogen Energy 42 (4), 1962–1969.
Zhang, Z., Shao, S. Dang J., Lu, c., Qin, F., Guan, W., 2017b. Synthesis of $ZnWO_4$/Ag_3PO_4 p-n heterojunction photocatalyst and enhanced visible-light photocatalytic applications. Water Sci. Technol. 77 (5-6), 1204–1212.
Zhao, Z., Zhang, B., Chen, D., Guo, Z., Peng, Z., 2016. Simultaneous reduction of vanadium (V) and chromium (VI) in wastewater by nanosized $ZnWO_4$ photocatalysis. J. Nanosci. Nanotechnol. 16 (3), 2847–2852.
Zhao, J., Yan, X., Zhao, N., Li, X., Lu, B., Zhang, X., Yu, H., 2018. Cocatalyst designing: a binary noble-metal-free cocatalyst system consisting of $ZnIn_2S_4$ and $In(OH)_3$ for efficient visible-light photocatalytic water splitting. RSC Adv. 8 (9), 4979–4986.
Zhao, G., Zou, J., Chen, X., Zhang, T., Yu, J., Zhou, S., Li, C., Jiao, F., 2020. Integration of microfiltration and visible-light-driven photocatalysis on a $ZnWO_4$ nanoparticle/nickel–aluminum-layered double hydroxide membrane for enhanced water purification. Ind. Eng. Chem. Res. 59 (14), 6479–6487.
Zhu, P., Nair, A.S., Shengjie, P., Shengyuan, Y., Ramakrishna, S., 2012. Facile fabrication of TiO_2–graphene composite with enhanced photovoltaic and photocatalytic properties by electrospinning. ACS Appl. Mater. Interfaces 4 (2), 581–585.